Universiteit Utrecht

Faculteit Bètawetenschappen

Bachelor Thesis

Fundamental physics with gravitational waves: LIGO/VIRGO versus Einstein Telescope

Author:

Q. Lafleur
Natuur- en Sterrenkunde

Supervisor:

Prof. dr. C.F.F. van den Broeck
Institute for Subatomic Physics

Utrecht, June 12, 2020

Abstract

With the construction of third generation gravitational wave detectors, gravitational wave physics will be taken to the next level. The Einstein Telescope is one of these third generation detectors, which could be operating in Europe by the mid 2030s. In this thesis we will analyse to what extent ET improves on current second generation detectors, using the Fisher matrix, regarding: (i) testing the strong-field regime of general relativity and (ii) constraining the neutron star equation of state.

Contents

1   INTRODUCTION

Second generation (2G) detectors, Advanced LIGO (AdLIGO) and Advanced VIRGO (Ad-VIRGO), have explored the Universe with gravitational waves (GWs) and produced extraordinary results in the last five years. Especially the first detections of GWs, originating from a binary black hole (BBH) [GW150914] [1] and a binary neutron star (BNS) [GW170817] [2], can be deemed historical and have resulted in a significant contribution to our knowledge concerning astrophysics, fundamental physics and cosmology [3]. In the upcoming decade the construction of the Einstein Telescope (ET), a third generation (3G) detector, will begin, which will have an order of magnitude increase in sensitivity and wider frequency bandwidth relative to its predecessors. This will allow us to take the exploration of the Universe with GWs to the next level.

In this thesis we explore how these improvements are made and their resulting implications related to two key issues concerning fundamental physics. We analyse to what extent the 3G detector ET improves on current 2G detectors, regarding the following subjects: (i) testing the strong-field regime of general relativity (GR) and (ii) constraining the NS equation of state (EOS).

We do this by executing an analysis based on the Fisher matrix that allows us to, roughly, estimate bounds on parameter estimation for current and future detectors. This is a rough but useful analysis technique when looking ahead at 3G detectors, since other possible, more accurate and data based techniques can not process ET signals, due to their long lasting presence (as long as 5 days) in the detection band [4]. The Fisher matrix does not use simulated or real data but is a Bayesian statistical analysis.

This thesis is divided into the following chapters.

In chapter 2 we derive the restricted PN waveform used in our analysis. Chapter 3 focuses on the main sources of noise that have been reduced for 3G detectors relative to 2G detectors, how this has been achieved and the noise power spectral density (PSD) (i.e. a measure for the sensitivity of a detector). In chapter 4 the Fisher formalism, which we use for estimating bounds on parameter estimation, is discussed, in combination with its limitations. Chapter 5 generalises the Fisher formalism to a network of detectors, to make it applicable to ET. In chapter 6 and 7 all previous chapters are combined and applied to two problems relating to fundamental physics.

In chapter 6 we analyse to what extent *deviations from GR* are measurable with future 3G detectors. We execute this analysis by first comparing extensive analyses by [5, 6], done with real data from AdLIGO/AdVIRGO, to our own Fisher analysis based on AdLIGO, to acquire knowledge of the offsets and biases associated with our Fisher formalism, which have to be taken into account. Thereafter we execute our analysis based on ET, with the acquired knowledge of the errors associated with our Fisher formalism in the back of our minds, to subsequently compare these ET results to the results obtained by the 2G extensive analyses. By this comparison we acquire knowledge of the improved accuracy that can be expected from ET, concerning the measurability of deviations from GR.

In chapter 7 we generally follow the same structure. We analyse to what extent *knowledge of the EOS coefficients*, related to the NS EOS, can be acquired with future 3G detectors. We first compare our Fisher analysis to an extensive analysis by [7], done with implemented sim-

ulated data resembling AdLIGO/AdVIRGO, to acquire knowledge of the offsets and biases associated with our Fisher formalism, which have to be taken into account. Thereafter we execute our analysis based on ET, again with the errors associated with the Fisher formalism in the back of our minds, to subsequently compare this with the results obtained by the extensive analysis. By comparing these two we acquire knowledge of the improved accuracy that can be expected from ET, concerning the measurement of EOS coefficients. We end with a summary of our conclusions, a discussion and an outlook for the future.

2   GRAVITATIONAL WAVES FROM COALESCING COMPACT BINARIES

2.1   The quadrupole formula

After deriving wavelike solutions to GR in his paper *'Näherungsweise Integration der Feldgleichungen der Gravitation'*(1916), which would travel with the speed of light and 'stretch and squeeze' spacetime, Einstein derived the following quadrupole formula for gravitational radiation from the general solution to linear GR [8]. This equation tells us that the second time derivative of the quadrupole moment of the GW source is proportional to the amplitude of the GW h_{ij} [8]:

$$h_{ij}^{TT}(t) = \frac{2G}{rc^4}\ddot{M}_{ij}^{TT}(t_{ret}),\tag{1}$$

with r being the distance to the source, G the gravitation constant, c the speed of light and M_{ij} the quadrupole moment of the source in the non-relativistic limit and TT gauge:

$$M_{ij}^{TT}(t_{ret}) = \frac{1}{c^2}\int_V \rho(t_{ret},\mathbf{x})x^i x^j dV_0,\tag{2}$$

with ρ the density of matter in a volume dV_0, x^i and x^j the coordinates of the components of the binary and $t_{ret} = t - \frac{r}{c}$. This result is derived under the assumption that the distance to the source r is a lot larger than the characteristic size of the source R: $r \gg R$.

2.2   Signal from inspiralling compact binary

By looking at Eq. (1), we can comprehend that GWs will originate from anything with a non-zero third time derivative of the quadrupole moment. Ordinary binary star systems seem to meet this requirement, but because of GWs being very hard to detect because of their "weak coupling to matter" [9], we will be looking at binary systems a lot more compact and disruptive to spacetime than ordinary binaries, such as BBHs and binary neutron stars BNSs.

To lowest order, an inspiralling compact binary system can be described as two point particles orbiting each other and losing energy due to the GWs they emit. Since this calculation has appeared in various papers, we will be brief and refer to [10–12] for a detailed calculation. The motion of two point particles, orbiting each other at a large distance R and with orbiting frequency ω_{orb}, can be described by a one-body model with the total mass M at the origin and the reduced mass μ orbiting the total mass.

By computing Eq. (1) for the above described one-body problem, while using energy conservation, Kepler's third law and the fact that the GW amplitude in the TT gauge is a combination of a cross ($h_\times$) and plus (h_+), we are able to compute two equations for $h_\times(t)$ and $h_+(t)$:

$$h_+(t) = \frac{4}{r}\left(\frac{G\mathcal{M}_c}{c^2}\right)^{5/3}\left(\frac{\pi f_{\mathrm{gw}}(t_{\mathrm{ret}})}{c}\right)^{2/3}\frac{1+\cos^2(\iota)}{2}\cos\left(\Phi\left(t_{\mathrm{ret}}\right)\right),\tag{3}$$

$$h_\times(t) = \frac{4}{r} \left(\frac{G\mathcal{M}_c}{c^2}\right)^{5/3} \left(\frac{\pi f_{\text{gw}}\left(t_{\text{ret}}\right)}{c}\right)^{2/3} \cos^2(\iota) \sin\left(\Phi\left(t_{\text{ret}}\right)\right),\tag{4}$$

with $\mathcal{M}_\lrcorner = \frac{(M_1 M_2)^{3/5}}{(M_1+M_2)^{1/5}}$, ι the inclination angle, $\Phi(t) = \int^t dt'\omega_{\text{gw}}\left(t'\right)$ the phase of the waveform and $f_{gw} = \omega_{orb}/\pi = 2f_{orb}$ [11]. [1]

The two polarisation equations described in Eqs. (3) and (4) induce a measured strain $h(t)$ in a GW detector, following [13]:

$$h(t) = F_+(\theta,\phi,\psi)h_+(t) + F_\times(\theta,\phi,\psi)h_\times(t),\tag{5}$$

with the following antenna pattern functions for the two polarisations:

$$F_+(\theta,\phi,\psi) = \frac{1}{2}\left(1+\cos^2\theta\right)\cos 2\phi\cos 2\psi - \cos\theta\sin 2\phi\sin 2\psi,\tag{6}$$

and

$$F_\times(\theta,\phi,\psi) = \frac{1}{2}\left(1+\cos^2\theta\right)\cos 2\phi\sin 2\psi + \cos\theta\sin 2\phi\cos 2\psi,\tag{7}$$

where θ, ϕ and ψ, together with the earlier defined ι, describe the orientation of the binary. For a visualisation of these angles, see figure 1.
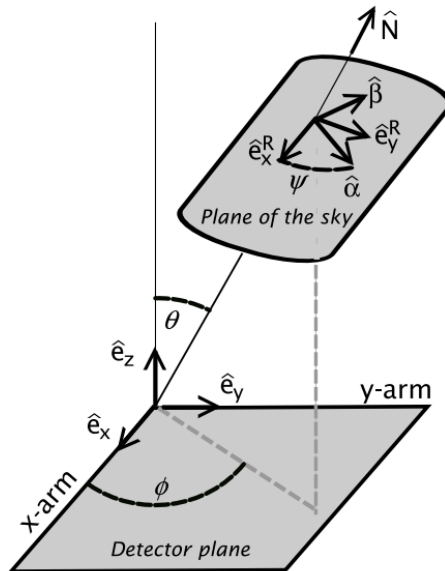
Figure 1: The relative orientation of the detector and sky frame [13].

We end up with an equation for the strain that describes, to lowest order, the detected waveform produced by inspiralling compact binaries [10]:

$$h(t) = A(t)\sqrt{F_+^2\left(1+\cos^2(\iota)\right)^2 + F_\times^2 4\cos^2(\iota)}\cos\left(\Phi(t)+\varphi_0\right),\tag{8}$$

with:

$$A(t) = \frac{4}{r}\left(\frac{G\mathcal{M}_c}{c^2}\right)^{5/3}\left(\frac{\pi f_{\text{gw}}\left(t_{\text{ret}}\right)}{c}\right)^{2/3}.\tag{9}$$

---

[1]Because of the quadrupolar property of GWs.

2.3 The stationary phase approximation

Because of later convenience and necessity concerning the Fisher matrix, we will be moving our waveform from the time-domain to the frequency domain with the help of a Fourier transform. Doing this analytically will necessitate an approximation called: the stationary phase approximation (SPA). We will be following earlier work [10], where the SPA was first introduced. This approximation considers only the stationary part of $\Phi(t)$ as this contributes the leading term to the integral and neglects the oscillating term, which is sub-leading. The Fourier transform of Eq. (8) can, according to the SPA, be written as:

$$
\int dt A(t) \cos\left(\Phi(t) + \varphi_0\right) e^{2\pi i f t} = \frac{1}{2} \int dt A(t) \left(e^{i(\Phi(t)+\varphi_0)} + e^{-i(\Phi(t)+\varphi_0)}\right) e^{2\pi i f t}
$$
$$
\simeq \frac{1}{2} e^{-i\varphi_0} \int dt A(t) e^{i(2\pi f t - \Phi(t))}.
$$
(10)

In Eq. (10) we have used Euler's formula to write $\cos\left(\Phi(t) + \varphi_0\right)$ in powers of e and we have neglected the oscillating term. The leading term in the integral comes from the stationary point: $t = t_s$ where $2\pi f = \dot{\Phi}(t_s)$. We have not included the orientation of the binary, as it is not affected by the Fourier transform. After doing a Taylor expansion on the exponent around $t = t_s$ we arrive at a frequency dependent phase:

$$
\Psi(f) = 2\pi f t(f) - \Phi(t(f)) - \frac{\pi}{4}.
$$
(11)

An equation for $f(t)$ can be found by realising that there is a balance between the change in emitted energy through the emission of GWs and the change in orbital energy ($\frac{dE_{\mathrm{GW}}}{dt} = -\frac{dE_{\mathrm{orb}}}{dt}$). This insight, combined with the knowledge of E_{orb} through Kepler's third law and E_{GW} through the stress-energy tensor [13], will give us an equation for the frequency evolution. This can be rewritten as [11]:

$$
t(f) = t_{\mathrm{coal}} - \frac{5}{256} \left(\frac{G\mathcal{M}_c}{c^3}\right)^{-5/3} (\pi f)^{-8/3},
$$
(12)

with t_{coal} the time at which collision takes place: $R \to 0$. When Eq. (12) is subsequently substituted in the definition of $\Phi(t)$ from section 2.2, this results in:

$$
\Phi(t) = -2 \left(\frac{5G\mathcal{M}_c}{c^3}\right)^{-5/8} \tau^{5/8}(t) + \Phi_c,
$$
(13)

with $\tau(t) = t_{\mathrm{coal}} - t$ and $\Phi_c = \Phi(t_{coal})$.

Having all of the components of the frequency dependent phase, we are now able to formulate the frequency dependent strain, to lowest order, for inspiralling compact binaries:

$$
\tilde{h}(f) = \sqrt{F_+^2 \left(1 + \cos^2(\iota) + F_\times^2 4\cos^2(\iota)\right)} \sqrt{\frac{5\pi}{96}} \frac{1}{(\pi f)^{7/6}} \frac{c}{r} \left(\frac{G\mathcal{M}_c}{c^3}\right)^{5/6}
$$
$$
\exp\left[i\left(2\pi f t_{\mathrm{coal}} - \Phi_{\mathrm{coal}} - \frac{\pi}{4} + \frac{3}{4}\left(\frac{8\pi G\mathcal{M}_c f}{c^3}\right)^{-5/3}\right)\right].
$$
(14)

As the waveform formulated in Eq. (14) only describes the circular inspiral of a compact binary, there must be a finite frequency at which the equation becomes invalid. This happens at the end of 'quasi-circular inspiral', where 'late inspiral' starts, which is, as can be seen in figure 2, followed by 'plunge and merger' and subsequently by 'ringdown' in the case of a BBH and 'post-merger' in the case of a BNS. This transition takes place near the location of the innermost stable circular orbit, which is approximately, in the case of our earlier described system, at $r_{ISCO} = \frac{6GM}{c^2}$ and at $f_{ISCO} = \frac{c^3}{6^{3/2}\pi MG}$ [14].
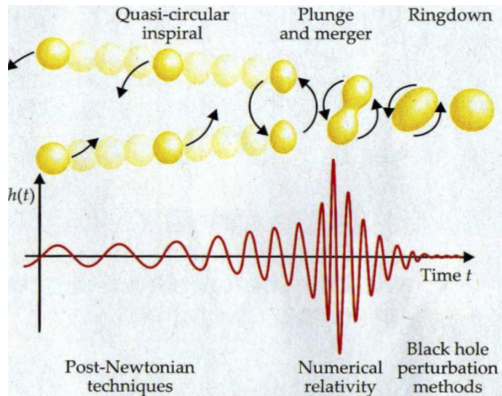

Figure 2: $h(t)$ evolution for inspiral, merger and ring down (IMR) [in red] in the case of a binary black hole [15].

2.4   The post-Newtonian formalism

Eq. (14) does a fine job in describing a system for the first stages of inspiral. But as the two objects in the binary lose orbital energy in the form of gravitational radiation, their separation will decrease, with an increase in orbital frequency as a consequence. With the binary being in the relativistic regime of GR for this part of inspiral, we will have to include higher-order terms that make Eq. (14) applicable to this relativistic regime [11].

Because we can consider the inspiral of a compact binary as adiabatic: $\omega^2 \gg \dot{\omega}$, we are allowed to expand our Eq. (14) with a power series in v/c, [2] called the post-Newtonian (PN) formalism [16], with v being the orbital velocity inside the system. This formalism is widely used to accurately describe the GWs created by inspiralling compact binaries, visualised in figure 2, up till the last stable circular orbit.

As in [16], we will be using the restricted PN waveform, which includes PN corrections to the phase up to 3.5PN order[3], but does not include any higher order corrections to the amplitude. This results in the following waveform, which is of similar shape as Eq. (14):

$$\tilde{h}(f) = \mathcal{A}f^{-7/6}e^{i\Psi(f)}, \tag{15}$$

with $\mathcal{A}$ being equal to the amplitude to 0PN, as derived in section 2.3, and the phase $\Psi(f)$ being of the following form, due to the expansion up to 3.5PN order (we will be putting

---

[2] As we assume that the orbital velocity v will always be a lot smaller than the speed of light c
[3] Up to 3.5PN order means up till $(v/c)^7$. Generally applies: $(v/c)^n$ corresponds to $n/2$PN order.

$c = G = 1$ from now on, to create more organised equations):

$$\Psi(f) = 2\pi f t_{coal} - \phi_{coal} - \frac{\pi}{4} + \frac{3}{128\eta v^5}$$

$$\left(\alpha_0 + v\alpha_1 + v^2\alpha_2 + v^3\alpha_3 + v^4\alpha_4 + v^5\alpha_5 + v^5 \log\left(\frac{v}{v_{ISCO}}\right)\alpha_{l5} + v^6\alpha_6 + v^6 \log(v)\alpha_{l6} + v^7\alpha_7 \right),$$

(16)

with $v = (\pi M f)^{1/3}$, $\eta = \frac{m_1 m_2}{M^2}$, $v_{ISCO} = (\pi M f_{ISCO})^{1/3}$ and the α coefficients, where α_{l5} and α_{l6} denote coefficients dependent on the logarithm of v:

$$\alpha_0 = 1, \tag{17}$$

$$\alpha_1 = 0, \tag{18}$$

$$\alpha_2 = \frac{20}{9}\left(\frac{743}{336} + \frac{11}{4}\eta\right), \tag{19}$$

$$\alpha_3 = -16\pi, \tag{20}$$

$$\alpha_4 = 10\left(\frac{3058673}{1016064} + \frac{5429}{1008}\eta + \frac{617}{144}\eta^2\right), \tag{21}$$

$$\alpha_5 = \pi(\frac{38645}{756} - \frac{65}{9}\eta), \tag{22}$$

$$\alpha_{15} = \pi(\frac{38645}{252} - \frac{65}{3}\eta), \tag{23}$$

$$\alpha_6 = \left(\frac{11583231236531}{4694215680} - \frac{640\pi^2}{3} - \frac{6848\gamma}{21}\right) + \eta\left(-\frac{15335597827}{3048192} + \frac{2255\pi^2}{12} + \frac{47324}{63} - \frac{7948}{9}\right) \tag{24}$$

$$+ \frac{76055}{1728}\eta^2 - \frac{127825}{1296}\eta^3 - \frac{6848}{21}\log(4), \tag{25}$$

$$\alpha_{l6} = -\frac{6848}{21}, \tag{26}$$

$$\alpha_7 = \pi\left(\frac{77096675}{254016} + \frac{378515}{1512}\eta - \frac{74045}{756}\eta^2\right), \tag{27}$$

$$\tag{28}$$

with $\gamma \approx 0.57721$, being the Euler-Mascheroni constant.

3   GRAVITATIONAL WAVE DETECTORS

GWs 'stretch and squeeze' spacetime maximally by 1 part in 10^{21} [13]. The development of detectors capable of measuring changes this small, has been strived for for decades by various GW organisations. This long-awaited sensitivity has eventually been achieved with the use of interferometric detectors similar to the Michelson interferometer, which was used in the historic Michelson-Morley-experiment. In the following chapter we will discuss: (i) the basic functioning of interferometric detectors, (ii) the main sources of noise an interferometric detector has to endure, (iii) second generation detectors, (iv) third generation detectors and (v) a comparison between these latter two.

3.1   Interferometric detectors

In an interferometer, the interaction between a laser beam and a GW is monitored by measuring changes in length using two perpendicular arms.
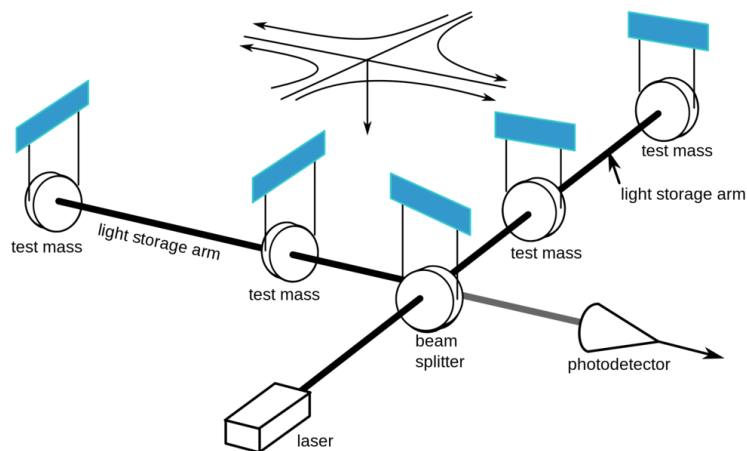
Figure 3: A schematic representation of an interferometer used in the detection of GWs. A beam of light with constant wavelength leaves the laser and is split by the beam splitter into two beams moving along the two perpendicular arms. The laser beam moves through the partially reflecting mirror located at the first test mass and is reflected from the mirror located at the second test mass. The beam will move back and forth between the two test masses multiple times (Fabry-Perot cavities) to eventually be recombined with the beam in the perpendicular arm at the beam splitter. The interference pattern of the beams will be detected by the photon detector [17].

When a GW hits earth, it 'stretches and squeezes' spacetime that will, subsequently, result in varying lengths of the two detector arms. The presence of such radiation can be detected using the interference characteristics of light. When gravitational radiation is absent, the beams in the two arms will not experience a phase shift relative to each other and will interfere constructively. But, when there is gravitational radiation present, one arm will stretch relative to the other and the enlarged distance the light travels in the stretched arm will

result in a relative phase shift and destructive interference consequently [9].[4]

Imagine now an interferometer with 4 km long arms, responding to a GW with an amplitude of around 10^{-21}. According to $h \sim \frac{\Delta L}{L}$, this will result in $\Delta L \sim 4 \times 10^{-18}$ m. To increase the change in measured distance ΔL, the path length L is increased by trapping the beam in the light storage arms, see figure 3, for example for 10 trips, resulting in an effective path length L_{eff} of 40 km [13]. This increases ΔL to approximately 4×10^{-17} m, which is still only one part in 10^{11} of a wavelength of light, in the case of light with a wavelength of 10^{-6} m, as used in modern-day interferometers [19].
Ground-based GW detectors have, in principle, the potential of sufficient sensitivity in the frequency domain: $[1, 10^4]$ Hz [13]. Below this domain they are fundamentally limited by noise sources inextricably linked to earth, such as seismic noise and gravity gradient noise that are too substantial at frequencies below 1 Hz. This results in the detectability of compact binaries with total masses up to $\approx 4 \times 10^3 M_\odot$ for ground-based detectors, when only considering early-inspiral and according to the in section 2.3 defined Eq. for f_{ISCO}.
Above this domain GW detectors are limited by the effective path length the light travels in the detector arms. For an interferometer to be sensitive to the passing by of GWs, spacetime should not change significantly while a beam of light is moving through an arm of the interferometer. I.e. the wavelength of the GW needs to be larger than the effective path length of the detector ($\lambda_{GW} > L_{eff}$), otherwise the stretching and squeezing of spacetime will take place multiple times and the effect of the GW will average out. This results in a maximal detectable GW frequency of 7500 Hz, in the case of an effective path length of 40 km.[5] There are however no detectable GW sources known that produce $f_{GW} > 5000$ Hz, so this limit to the sensitivity band does not limit the detections possible with modern day interferometers. Only when the effective path length is made incredibly long, as is planned for future space based detectors, higher frequency sources will cease to be detectable [12].

3.2 Understanding the noise

Measuring distances, in the order of 10^{-17} m with 10^{-6} m wavelength of light, is, understandably, an incredibly hard task. Particularly in the light of the multiple sources of noise that are part of living on earth. Controlling and identifying these various sources of noise is key to the measurement of GWs. This section will be dedicated to the main sources of noise present in interferometers. We will be following earlier work [13].

3.2.1 Seismic noise

Seismic noise is mostly caused by sources such as earthquakes, wind, micro seismic events and various kinds of anthropogenic noise. Below 50 Hz they form one of the main limiting factors to the sensitivity of an interferometer and below 1 Hz they are deemed too substantial for ground-based detectors, to detect GWs below this threshold [20]. The amount of seismic

---

[4]In reality, GW detectors often reverse this procedure: when there is no gravitational radiation present, the beams will cancel each other out and when there is gravitational radiation present, the beams will constructively interfere [18].
[5]According to $\lambda_{GW} = c/f_{GW}$.

noise in the system gets enlarged with every reflection of the beam of light with a slightly vibrating mirror. To counter this, interferometers make use of the filtering properties of pendulums for frequencies above their natural frequency, which is at a few Hertz in the case of a 0.5 m pendulum. As a consequence mirrors are hung on pendulums that filter the seismic noise subsequently [13].

3.2.2   Thermal noise

Thermal noise is a form of random fluctuations driven by thermal energy. These random fluctuations can cause vibrations in the, in section 3.2.1 described, pendulums and the wires connecting the pendulums to the mirrors. As with seismic noise, the total amount of thermal noise in the system gets enlarged with every reflection of the beam of light. The amplitude of the vibrations is largest at the resonant frequencies of the components of the suspensions: the pendulums (at a few Hz) and the wires connecting the pendulums with the mirrors (at ≈ 1 kHz).[6] These unwanted vibrations are called suspension thermal noise [13]. By using materials with high Q-factors, the thermal vibrations in the suspensions are confined to a small bandwidth around the resonant frequency, because of the relation: $Q = \frac{f_r}{\Delta f}$ [21], with f_r the resonant frequency and Δf a measure of the bandwidth around the resonant frequency.[7] The suspension thermal noise can be reduced by the usage of high Q-factored materials, avoiding the resonant frequencies during measurements and lowering the temperature [22].

Thermal noise can also cause random fluctuations in the index of refraction. When the light beam gets partly transmitted by a beam splitter or partly reflecting mirror, a small amount of energy is absorbed by the mirror, which causes the mirror to rise in temperature and change its index of refraction. As these thermal fluctuations vary over time, the index of refraction changes accordingly. This type of noise is called test mass thermal noise. These changes in optical properties can be reduced by using less laser power, as this produces less heating, lowering the temperature or usage of high Q-factor materials [13].

3.2.3   Quantum shot noise

Due to quantisation, light leaves the laser in discrete chunks: photons. This causes random fluctuations in the light intensity (i.e. amplitude) measured by the detector. The error in these fluctuations goes like: $\Delta l_{shot} \sim \frac{1}{\sqrt{N}}$ with N the amount of photons. By shooting more photons (the laser power in modern-day interferometers builds up to ≈ 1 MW in the cavities) [23], the uncertainty in the fluctuations becomes smaller. This makes it less likely that a random fluctuation in the light intensity is recognised as a GW [13].

3.2.4   Quantum radiation pressure noise

Because of the quantum nature of shot noise and the Heisenberg uncertainly principle, the reduction of shot noise by the increase of laser power, goes hand in hand with the increase in quantum radiation pressure noise. The high-power laser beam transfers a slightly fluctuating

---

[6]These are also called violin-modes.

[7]This is called the full width at half maximum FWHM.

momentum onto the suspended test masses that are free to move under radiation pressure. This quantum radiation pressure varies due to the uncertainty principle imposed by quantum mechanics and creates a varying disturbance accordingly, which creates a phase shift that can mask a GW [13].

But, as we are not trying to measure the phase and the amplitude at once, it is possible to try and 'squeeze' all the quantum uncertainty into the variable that is not measured, to 'relieve' the measured variable from its uncertainty. This is done with the help of 'squeezed light' that has a phase with a reduced quantum uncertainty relative to its coherent amplitude, or the other way round. When 'squeezed light' is made frequency dependent, quantum shot noise and quantum radiation pressure noise can be reduced simultaneously. How this works in detail does not fall within the scope of this paper. Extensive research on 'squeezed light' will be done by Dutch organisations: Nikhef and Maastricht University, with help of the prototype: ET Pathfinder, which is currently being build. For more information on squeezed light or the ET Pathfinder, see [24–26].

3.2.5   Gravity gradient noise

Another form of seismic noise, which is different from the earlier described seismic noise, is called: gravity gradient noise. With the passing of seismic waves near a GW detector, there are perturbations created in the density of the earth that subsequently create a fluctuating gravitational pull on the test masses inside the arms of the interferometer [13, 27]. Time dependent density fluctuations in the atmosphere can excite a similar force on the test masses. These fluctuations are particularly noticeable at lower frequencies but fall of at a few Hz. Gravity gradient noise is very hard to reduce. Sufficient sensitivity for the detection of GWs below 1 Hz would necessitate a sky-based interferometer, but the fabrication of detectors in quiet underground locations (e.g. ET) could already help significantly in the $[1, 10]$ Hz regime, as this reduces the initial seismic excitation [28].

3.2.6   Gas noise

The presence of gas molecules causes another kind of noise that will have to be dealt with: gas noise in the form of displacement noise and sensing noise. The former originates from the movement of molecules due to thermal energy and the subsequent exchange of momentum with the test masses, which results in a shift in phase of the light beam. The latter originates from the present gas molecules interacting with the photons of the light beam, which also results in an optical phase shift of the light beam. Creating vacuum arms helps to overcome this problem [29].

3.3   Second generation detectors: AdLIGO, AdVIRGO

The two Advanced LIGO detectors and the Advanced VIRGO detector are, till this day, the only detectors that have detected GWs. All three are variants of the, in section 3.1 described, interferometers (Fabry-Perot Michelson interferometer) with arm-lengths of 4 km in the case of AdLIGO and 3 km in the case of AdVIRGO. With help of section 3.2, we can analyse
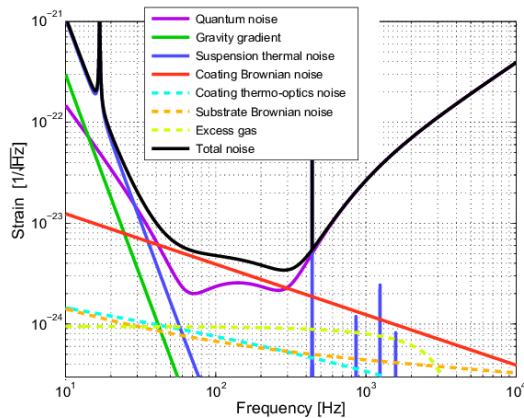
figures 4 and 5.

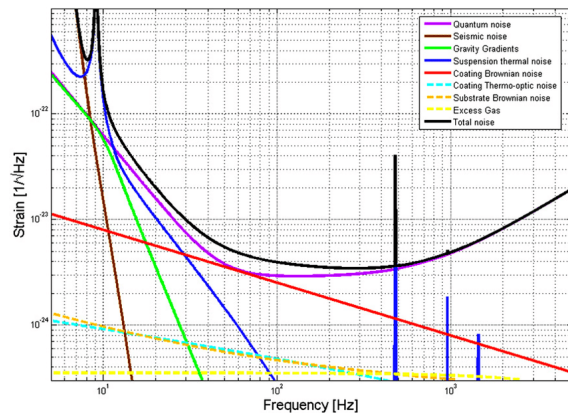Figure 4: Noise budget AdVIRGO [30].

Figure 5: Noise budget AdLIGO [31].

Figure 6: The noise budgets of AdVIRGO and the two AdLIGO detectors at design sensitivity, with on the horizontal axis: the frequency [Hz] and on the vertical axis the spectral amplitude: $\tilde{h}(f)/\sqrt{Hz}$ $[1/\sqrt{Hz}]$, which is a measure for the sensitivity of the detector. The principle noise curves are plotted that reduce the detector sensitivity. To convert to the RMS strain in a domain, you multiply the spectral amplitude by the square root of the bandwidth. At 200 Hz with a bandwidth of 100 Hz, AdLIGO has a spectral amplitude of approximately $3 \times 10^{-24}[1/\sqrt{Hz}]$ and a resulting RMS detector sensitivity of approximately 3×10^{-23}.

Both AdLIGO and AdVIRGO experience their peak sensitivity at frequencies in the bandwidth $[100, 300]$ Hz. At frequencies above this domain the sensitivity of both detectors is limited by quantum shot noise. The other source of quantum noise: radiation pressure noise, limits both detectors in the $[10, 100]$ Hz regime. Reducing the high frequency shot noise is possible by increasing the laser power, but at the expense of increasing the radiation pressure noise. Together they form the quantum limit, see sections 3.2.3 and 3.2.4.

Gravity gradient noise creates a hard limit on sensitivity at 10 Hz for above ground, ground-based detectors, as discussed in section 3.2.5, which results in 10 Hz being the lower cutoff frequency.

There are many ways in which thermal noise is present, but not all limit the sensitivity of the detector. A peak in suspension thermal noise in the $[10, 20]$ Hz domain does limit the sensitivity and originates from the resonant frequency of the suspension pendulums. Multiple other peaks are visible in figure 4 at frequencies around 1000 Hz that originate from the suspension wires, but as these peaks span only a narrow frequency band, they are easily removed from the data. Coating Brownian noise, coating thermo-optic noise and substrate Brownian noise are all forms of test mass thermal noise. Only coating Brownian noise has any significance, which arises from "mechanical dissipation in the coatings of the mirrors" [32]. The other terms are no limiting factors yet.[8]

---

[8]For more information about test mass thermal noise, visit [29].

Because of the use of isolating systems reducing seismic noise, seismic noise can be neglected below frequencies of 10 Hz.

As the arms of the detectors are vacuumed, there is little gas remaining that can interact with the measurement. There are, however, still some gas molecules present that cause the excess gas noise. AdLIGO and AdVIRGO have not yet arrived at sensitivities where this becomes a problem.

3.4   Third generation detector: ET

3G detectors will be needed to improve detector sensitivity even further. Einstein telescope (ET) is one of those 3G detectors planned for the future that will be a factor 10 more sensitive than the 2G detectors, reviewed in section 3.3, and will open up the $[1, 10]$ Hz frequency domain. This will make the observation of BBHs up to $\approx 4 \times 10^3 M_\odot$ possible, see section 3.1, and will make the observation time of stellar mass binaries, according to Eq. (12), significantly longer. A BNS consisting of two neutron stars with equal mass: $1.4 M_\odot$, would be in the AdLIGO observation band for approximately 15 minutes. They would be in the ET observation band (in the most optimistic case of $f_{cutoff} = 1$ Hz), for more than 5 days [33].
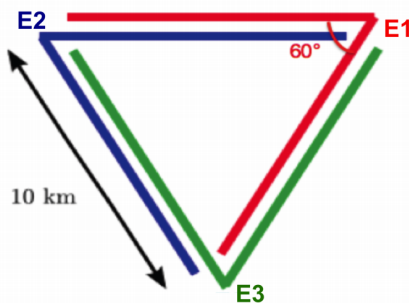
Figure 7: A schematic view of the planned Einstein Telescope. A total of 6 interferometers would cooperate to produce one GW detector [33].

ET is planned to be a combination of three Fabry-Perot Michelson interferometers, as described in section 3.2, but with V-shaped arms with 60° angles, arranged in a triangle, see figure 7. All arms will be 10 kilometers in length with in each V-shape two interferometers, one sensitive to lower frequencies and one sensitive to higher frequencies. ET will be build underground to reduce all sources of seismic noise.
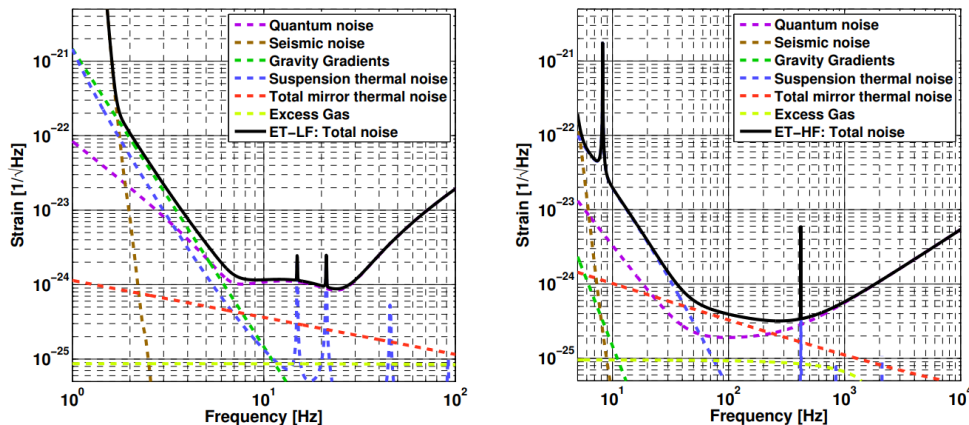
Figure 8: The noise budgets for the low and high frequency interferometers in ET at design sensitivity, with on the horizontal axis: the frequency [Hz] and on the vertical axis the spectral amplitude: $\tilde{h}(f)/\sqrt{Hz}$ $[1/\sqrt{Hz}]$, which is a measure of the sensitivity of the detector. The principle noise curves are plotted that reduce the detectors sensitivity. The two spectral amplitudes can be added in a way that the lowest spectral amplitude represents the sensitivity of the detector. To convert to the RMS strain in a domain, you multiply the spectral amplitude by the square root of the bandwidth. For example, at 200 Hz with a bandwidth of 100 Hz, ET-high has a spectral amplitude of approximately $2 \times 10^{-25}[1/\sqrt{Hz}]$ and a resulting RMS detector sensitivity of approximately 2×10^{-24} [28].

From figure 8, we can conclude that, when design sensitivity is reached, ET will have its intended sensitivity. The spectral amplitude visualised in figure 8 is, over its whole bandwidth, a 10 factor improvement relative to the 2G detectors and the spectral amplitude of ET stays below 10^{-22} for frequencies > 1 Hz.

Due to the combination of high-frequency interferometers (HFI) and low-frequency (LFI) interferometers, ET is able to lower both its quantum shot noise and its quantum radiation pressure noise by increasing the build up laser power in the HFI and reducing the build up laser power in the LFI, see sections 3.2.3 and 3.2.4. The power in the HFI cavities builds up to 3 MW, while the laser power in the LFI builds up to a modest 18 kW. Frequency-dependent squeezing of light helps to reduce all quantum noise sources even further, see section 3.2.4 [33]. Even though all these adjustments have been made, quantum noise still limits the HFI at $f > 500$ Hz and the LFI at $f > 7$ Hz.

The reduction of laser power in the LFI also reduces test mass thermal noise.[9] By operating the mirrors of the LFI at cryogenic temperatures (at $T \approx 10$ K) and by using silicon or sapphire because of their high Q-factors at low temperature, all thermal noise factors present in the LFI are reduced, see section 3.2.2 [34]. Test mass thermal noise is limiting the overall sensitivity of the HFI in the $[40, 200]$ Hz frequency domain.

Suspension thermal noise is thus reduced by cryogenic temperatures and high Q-factor materials in the LFI. However, suspension thermal noise does limit the sensitivity of the HFI

---

[9]This is called: total mirror thermal noise in figure 8.

in the $[4, 70]$ Hz domain because of HFI operating at room temperature. This is, however, irrelevant because of the LFI being more sensitive in this domain.

The sensitivity of the LFI below 7 Hz, is limited by seismic, gravity gradient, quantum radiation and suspension thermal noise by comparable amounts. The significant reduction of seismic and gravity gradient noise in this regime, relative to 2G detectors is due to the underground placement of this whole system of interferometers at a location with little seismic activity [34].

In ET there will be some excess gas present. This excess gas will, just like in adLIGO and AdVIRGO, produce no limiting factors to its sensitivity.

3.5   Overview detectors
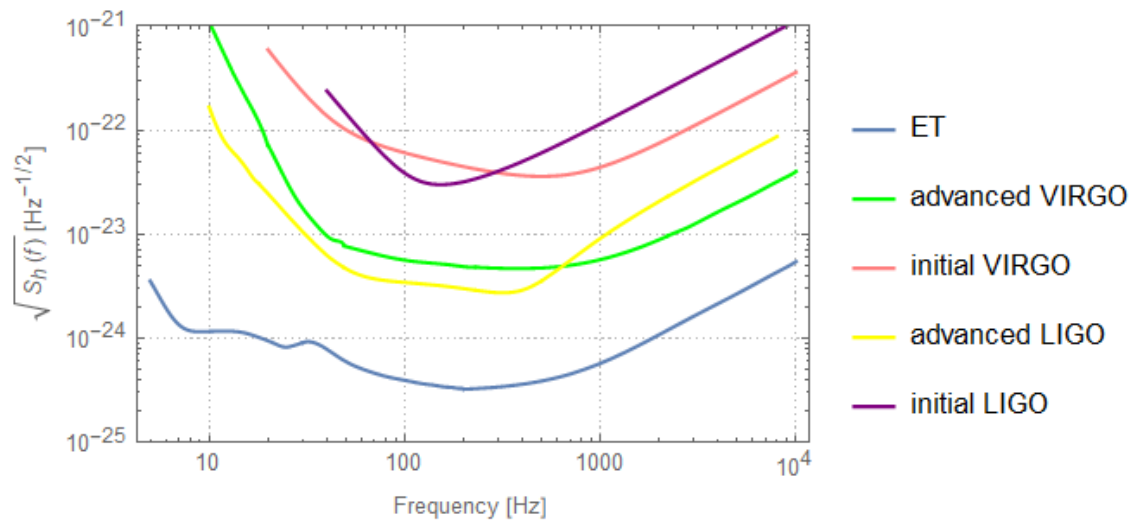
Figure 9: The sensitivities of first (initial LIGO and initial VIRGO [16]), second (AdVIRGO and AdLIGO [35]) and third (ET) [36] generation detectors. With on the horizontal axis: the frequency [Hz] and on the vertical axis: the square root of the noise power spectral density (PSD) (i.e. the spectral amplitude). The sensitivity plotted for ET describes a combination of one LFI and one HFI.

In figure 9, is clearly visible how every next generation detector has reduced in spectral amplitude by a factor of 10. The lower cutoff frequency has also been significantly reduced from 40 Hz for Initial LIGO to $[1, 5]$ Hz for ET.

One thing possible with help of the square of the spectral amplitude $S_h(f)$ (i.e. the noise power spectral density (PSD)), is determining the signal-to-noise ratio (SNR). Determining this ratio is done by combining the frequency dependent strain $\tilde{h}(f)$, derived in section 2.4, with the PSD in the following manner [16]:

$$SNR^2 = 4\Re \int_{f_s}^{f_{ISCO}} \frac{|\tilde{h}(f)|^2}{S_h(f)} df, \tag{29}$$

with f_s the lower cutoff frequency of the detector and f_{ISCO} defined as in section 2.3. We can clearly see that: a strong signal (i.e. a large amplitude $\mathcal{A}$ of $\tilde{h}(f)$) and a sensitive detector (i.e. a small PSD) result in a high SNR. The phase is irrelevant to the SNR, because of the absolute square present in the integral.

By looking at the amplitude of the waveform in Eq. (14), one can see that the strain falls of as r^{-1} that, subsequently, results in the SNR being proportional to r^{-1}, according to Eq. (29). If we assume now that GW sources are roughly evenly distributed through space, this results in $N \propto V \propto r^3 \propto SNR^{-3}$. Now we can determine an SNR probability distribution. In the local universe the amount of binaries within luminosity distance r_* is $N(r < r_*) \propto r_*^3$, or, when transcribed into SNRs: $N(SNR > SNR_*) \propto SNR_*^{-3}$. And subsequently an SNR probability distribution that scales like: $\frac{dN(SNR > SNR_*)}{dSNR_*} \propto SNR_*^{-4}$ [37]. A variety of SNR probability distributions is plotted in figure 11.
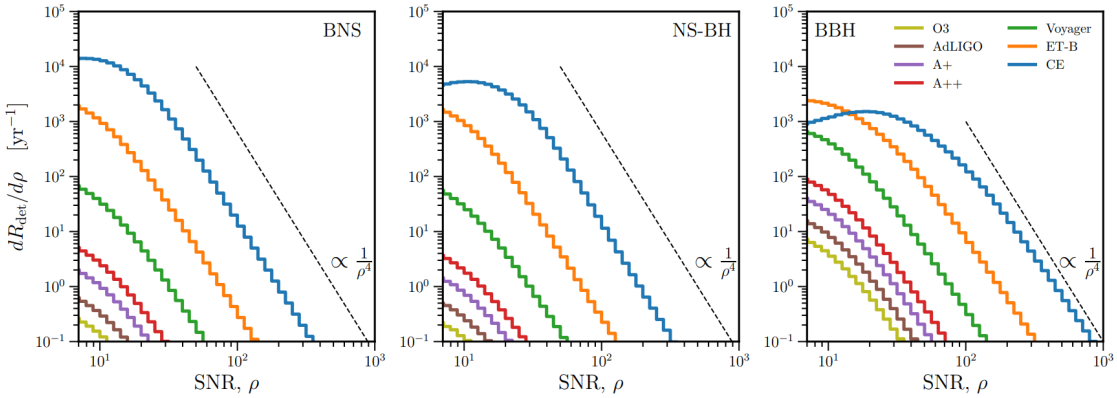
Figure 10: SNR probability distributions modelled for the detection of BNSs, NS-BHs and BBHs for different detectors: 03 is observation run 3 of AdLIGO, AdLIGO is AdLIGO at design sensitivity, A+ and A++ are potential future configurations for AdLIGO and the potential future generation detectors: Voyager, CE and ET-B, which was an early estimation of ET at design sensitivity. R_{det} is the amount of estimated detections per year for each given detector. Most of the binaries with very large SNRs are in the local universe, which results in them scaling like: $1/SNR^4$ [37].

Figure 11 tells us two things: (i) future 3G detectors will observe GW sources with significantly higher SNRs. ET will probably detect BNSs with $SNR > 100$ every year, while AdLIGO struggles even to detect one BNS with $SNR > 10$ every year. And (ii), because the surface below the graph indicates the amount of estimated detections per detector per year, the construction of 3G detectors will result in a more than significant increase in detections. ET will probably detect a factor 10^3 more BNSs, NSBHs and BBHs than AdLIGO.[10]

---

[10]For an overview of minimum and maximum detection rates per detector, see [37].

4   MEASURING THE PARAMETERS OF THE SOURCE

As, in this thesis, we are trying to determine to what degree the properties of GW sources are measurable using different detectors, we will in this chapter describe the derivation of a probability distribution for parameters that we can execute for current and future detectors. We will be following earlier work [11] combined with [12], for the coming sections 4.1 and 4.2.

4.1   The posterior density function

Imagine an experiment, in which data d is collected to determine the parameters θ, which describe the properties of the source. Now imagine, we would have a hypothesis H that describes the probability of getting d for given θ and general background information I.[11] Let us call this probability distribution the 'likelihood': $p(d|\theta, H, I)$. Where $p(A|B)$ describes the probability of A, given B is true.
We are however, as stated above, trying to determine the probability of getting parameters θ given data d, called the 'posterior probability density' or 'posterior density function' (PDF). This can be achieved with help of Bayes' theorem:

$$p(\theta|d, H, I) = \frac{p(d|\theta, H, I)p(\theta|H, I)}{p(d|H, I)},\tag{30}$$

where we also introduce: the 'prior probability density' $p(\theta|H, I)$ that describes our knowledge of the parameters θ before the experiment, and the 'evidence' $p(d|H, I)$, which is not relevant for our purpose as it is not dependent on θ and can be seen as a normalisation constant. This results in the following possible formulation of Bayes' theorem:

$$p(\theta|d, H, I) \propto p(d|\theta, H, I)p(\theta|H, I).\tag{31}$$

We can conclude from Eq. (35) that, when possessing prior knowledge of θ and a model H that describes the probability of getting d given θ, we are able to derive the PDF, which subsequently leads to an indication of to what extent the parameters of a source are measurable.

4.2   Derivation Fisher matrix

Let us first state that in the case of our GW analysis, the hypothesis H used, consists of a 'family of possible waveforms' that describe inspiral up to 3.5PN order, described as in section 2.4 and parameterised by source parameters θ and frequency f.
We consider a situation in which a GW is present in the data, so that the data $d(t)$ (i.e. the output of the detector) consists of a combination of intrinsic noise $n(t)$ and a GW signal $h(t; \vec{\theta})$, with $\vec{\theta} = (\theta^1, ..., \theta^k)$ being the unknown parameters of the source:

$$d(t) = n(t) + h(t; \vec{\theta}).\tag{32}$$

---

[11]As we are considering a 'joint probability distribution' this method is called a 'generative model'.

Next we assume that the noise $n(t)$ is a zero-mean, stationary[12] and Gaussian random process that has the following probability distribution for some noise realisation n:

$$p(n) \propto e^{-\frac{1}{2}(n|n)}, \tag{33}$$

where $(|)$ denotes the noise weighted inner product, defined as: $(g|h) = 4\Re \int_0^\infty df \frac{\bar{g}^*(f)\bar{h}(f)}{S_h(f)}$, with $\bar{h}$ the Fourier transform of h and $\bar{g}^*$ the complex conjugate of $\bar{g}$. $S_h(f)$ should come across as familiar regarding chapter 3, as a measure of the sensitivity of a detector (i.e. the PSD). An intuitive insight can be obtained from the way $S_h(f)$ is present in Eq. (33) regarding the general definition of a Gaussian distribution: $g(x) \propto e^{-\frac{1}{2}\left(\frac{x-\mu}{\sigma}\right)^2}$, with variance σ^2 and expected value μ. Comparing the general definition with Eq. (33) leads to the conclusion that $S_h(f)$ is a measure of the variance in the noise distribution at some frequency f and therefore a measure of the sensitivity of the detector at that frequency. The greater the spread in the noise distribution (and thus the greater S_h) at a particular frequency, the more random noise will be present and the less sensitive a detector will be.

Now, focusing again on determining the PDF, we can use Eq. (32) to determine the, in section 4.1 described likelihood. After rewriting Eq. (32) as: $n(t) = d(t) - h(t; \vec{\theta})$ and substituting this into Eq. (33) we end up with the likelihood:

$$p(d|\vec{\theta}, H, I) \propto e^{-\frac{1}{2}(d-h(\vec{\theta})|d-h(\vec{\theta}))}. \tag{34}$$

If we assume now the prior $p(\vec{\theta}|H)$ to be flat, i.e. uniformly distributed, we arrive at an expression proportional to the PDF:

$$p(\vec{\theta}|d, H, I) \propto e^{-\frac{1}{2}(d-h(\vec{\theta})|d-h(\vec{\theta}))}. \tag{35}$$

In Eq. (38), given data d, various combinations of particular noise realisations and particular waveforms are possible. The most likely waveform will result from the most likely noise realisation.

In general, the PDF gives us the probability of $\vec{\theta}$, which describes the probability of getting certain parameter values. This probability distribution is peaked at a certain maximum likelihood $\vec{\theta}_{ml}$, which is often not equal to the true parameters of the source due to some realisation of the noise. However, since we are not trying to determine the true parameter values, but only the width of their distribution when a source with parameter values equal to $\vec{\theta}_{ml}$ is detected, we still assume that:

$$\vec{\theta} = \vec{\theta}_{ML} + \delta\vec{\theta}, \tag{36}$$

with $\delta\vec{\theta}$ a small deviation.

Because of the irrelevance of defining a probability distribution for a stationary point, we now solely derive the probability distribution for $\delta\vec{\theta}$. We begin with writing out the inner product:[13]

$$p(\delta\vec{\theta}) \propto e^{-\frac{1}{2}(d-h(\vec{\theta})|d-h(\vec{\theta}))} \propto e^{-\frac{1}{2}(d|d)+(d|h(\vec{\theta}))-\frac{1}{2}(h(\vec{\theta})|h(\vec{\theta}))}. \tag{37}$$

---

[12]I.e. not time dependent.

[13]From now on, we will stop mentioning the prior knowledge.

After taking the logarithm, we end up with an equation we can work with:

$$\log(p(\delta\vec{\theta})) = (d|h(\vec{\theta})) - \frac{1}{2}(h(\vec{\theta})|h(\vec{\theta})) + C, \tag{38}$$

where C is an added constant comprised of the $(d|d)$ term and due to the shift from proportionality to equality.

We need two other equations to form Eq. (38) into something usable. Our first equation comes from the fact that we can Taylor expand $h(\vec{\theta})$ around $\vec{\theta}_{ML}$ in the following way:[14]

$$h(\vec{\theta}) = h(\vec{\theta}_{ML}) + \frac{\partial h(\vec{\theta}_{ML})}{\partial \theta^i}\delta\theta^i + \frac{1}{2}\frac{\partial^2 h(\vec{\theta}_{ML})}{\partial \theta^i \partial \theta^j}\delta\theta^i \delta\theta^j. \tag{39}$$

In addition we state that the derivative of Eq. (38) with respect to θ^i is zero at the point of maximum likelihood. This gives us the following equation:

$$\left.\frac{\partial \log(p(\delta\vec{\theta}))}{\partial \theta^i}\right|_{ML} = \left(d\Big|\frac{\partial h(\vec{\theta}_{ML})}{\partial \theta_i}\right) - \left(h(\theta_{ML})\Big|\frac{\partial h(\vec{\theta}_{ML})}{\partial \theta^i}\right) = 0. \tag{40}$$

If we now substitute Eq. (39) into Eq. (38), we can rewrite Eq. (38) in the following manner (the constant C will be dropped as we will switch back to proportionality):

$$\log(p(\delta\vec{\theta})) \propto (d|h(\vec{\theta})) - \frac{1}{2}(h(\vec{\theta})|h(\vec{\theta}))$$

$$= \left(d|h(\vec{\theta}_{ML})\right) + \left(d\Big|\frac{\partial h(\vec{\theta}_{ML})}{\partial \theta^i}\right)\delta\theta^i + \frac{1}{2}\left(d\Big|\frac{\partial^2 h(\vec{\theta}_{ML})}{\partial \theta^i \partial \theta^j}\right)\delta\theta^i \delta\theta^j - \frac{1}{2}\left(h(\vec{\theta}_{ML})|h(\vec{\theta}_{ML})\right)$$

$$- \left(h(\vec{\theta}_{ML})\Big|\frac{\partial h(\vec{\theta}_{ML})}{\partial \theta^i}\right)\delta\theta^i - \frac{1}{2}\left(h(\vec{\theta}_{ML})\Big|\frac{\partial^2 h(\vec{\theta}_{ML})}{\partial \theta^i \partial \theta^j}\right)\delta\theta^i \delta\theta^j - \frac{1}{2}\left(\frac{\partial h(\vec{\theta}_{ML})}{\partial \theta^i}\Big|\frac{\partial h(\vec{\theta}_{ML})}{\partial \theta^j}\right)\delta\theta^i \delta\theta^j. \tag{41}$$

By making use of Eq. (40) and by neglecting all inner products that are independent of $\delta\theta$, we can simplify Eq. (41) even further:

$$\log(p(\delta\vec{\theta})) \propto (d|h(\vec{\theta})) - \frac{1}{2}(h(\vec{\theta})|h(\vec{\theta}))$$

$$= \frac{1}{2}\left(d\Big|\frac{\partial^2 h(\vec{\theta}_{ML})}{\partial \theta^i \partial \theta^j}\right)\delta\theta^i \delta\theta^j - \frac{1}{2}\left(h(\vec{\theta}_{ML})\Big|\frac{\partial^2 h(\vec{\theta}_{ML})}{\partial \theta^i \partial \theta^j}\right)\delta\theta^i \delta\theta^j - \frac{1}{2}\left(\frac{\partial h(\vec{\theta}_{ML})}{\partial \theta^i}\Big|\frac{\partial h(\vec{\theta}_{ML})}{\partial \theta^j}\right)\delta\theta^i \delta\theta^j. \tag{42}$$

By combining the first and second inner product present in Eq. (42), with help of Eq. (32), we arrive at an expression for the PDF:

$$\log(p(\delta\vec{\theta})) \propto \frac{1}{2}\left(n\Big|\frac{\partial^2 h(\vec{\theta}_{ML})}{\partial \theta^i \partial \theta^j}\right)\delta\theta^i \delta\theta^j - \frac{1}{2}\left(\frac{\partial h(\vec{\theta}_{ML})}{\partial \theta^i}\Big|\frac{\partial h(\vec{\theta}_{ML})}{\partial \theta^j}\right)\delta\theta^i \delta\theta^j. \tag{43}$$

---

[14]Einstein summation convention has been used.

The PDF does still consist of two components that do not contribute in a similar manner to the PDF. We need to have a look at the SNR, described in Eq. (29), to see which term is more relevant.

When substituting the derived equation for the waveform up to 3.5PN order, described in Eq. (15), into Eq. (29), we see that the SNR is independent of Ψ because of the absolute square that is taken, and the amplitude squared $\mathcal{A}^2$ can be placed outside of the integral, because of it not being dependent on f. This results in the SNR being proportional to $\mathcal{A}$ (i.e. $SNR \propto \mathcal{A}$).

If we now focus again on Eq. (43), we can use this proportionality to state that the first term is proportional to $\mathcal{A}$ and thus to SNR, while the second term is proportional to $\mathcal{A}^2$ and thus to SNR^2. Based on the GW detections done by AdVIRGO and AdLIGO [5], a minimal SNR of 8 seems to be necessary for the detection of GWs. This leads us to conclude that in the case of high SNR, the second term will overshadow the first term and the following linearised-signal approximation LSA can be made (we will elaborate further on this approximation in the next section):

$$\log(p(\delta\vec{\theta})) \propto -\frac{1}{2}\left(\frac{\partial h(\vec{\theta}_{ML})}{\partial\theta^i}\Big|\frac{\partial h(\vec{\theta}_{ML})}{\partial\theta^j}\right)\delta\theta^i\delta\theta^j. \tag{44}$$

This in turn leads to the following useful expression:

$$p(\delta\vec{\theta}) \propto e^{-\frac{1}{2}\Gamma^{ij}\delta\theta^i\delta\theta^j}, \tag{45}$$

with Γ^{ij} being the so-called Fisher matrix, defined as the matrix of the noise weighted inner products:

$$\left(\frac{\partial h(\vec{\theta}_{ML})}{\partial\theta^i}\Big|\frac{\partial h(\vec{\theta}_{ML})}{\partial\theta^j}\right). \tag{46}$$

We can clearly see that the PDF described in Eq. (45) follows a Gaussian distribution, which is described earlier in this section, only in more than one dimension. This enables us to determine the spread of the multivariate distribution. When we set $i = j$, according to the definition of a Gaussian distribution, we can state that the spread for a single parameter can be derived from the Fisher matrix: $\sigma^i = \sqrt{(\Gamma^{ii})^{-1}}$. Generalising this and defining the inverse of the Fisher matrix as the variance-covariance matrix Σ^{ij}, gives us a matrix with on the diagonal the variance of each parameter [i.e. a measure for the uncertainties in the estimation of the parameters of the source] and on the off-diagonal elements the covariance between parameters. The diagonal elements, in which we are solely interested, are defined as follows:

$$\sigma^i = \sqrt{\Sigma^{ii}} \equiv \sqrt{(\Gamma^{ii})^{-1}} \tag{47}$$

Because of the earlier described proportionality of Γ^{ij} to SNR^2, σ^i (i.e. the RMS deviation of parameter θ^i from θ^i_{ML}) falls of as SNR^{-1}. This is why a higher SNR will result in more accurate measurements.

Achieving more accurate measurements can also be done by combining several PDFs with the same, or approximately the same, expectation value and spread:

$$p(\delta\theta^i) = \prod_{n=1}^{N} p(\delta\theta^i_n) \propto e^{-\frac{1}{2}\frac{\delta\theta^{i\,2}_1}{\sigma^{i\,2}_1}} e^{-\frac{1}{2}\frac{\delta\theta^{i\,2}_2}{\sigma^{i\,2}_2}}...e^{-\frac{1}{2}\frac{\delta\theta^{i\,2}_N}{\sigma^{i\,2}_N}} \propto e^{-\frac{1}{2}\frac{N\delta\theta^{i\,2}}{\sigma^{i\,2}}} \propto e^{-\frac{1}{2}\frac{\delta\theta^{i\,2}}{(\sigma^i/\sqrt{N})^2}} \tag{48}$$

This results, as can be seen in Eq. (48), in a decrease in spread by a factor $\sqrt{N}$.

A lot of approximations have been made in this section. Because of these approximations, the Fisher matrix breaks down in certain situations that will be highlighted in the next section.

4.3   The Fisher matrix: caveats

Let us first of all state that the Fisher matrix is a formalism with some limitations. The estimation of the spread in the maximum-likelihood parameter $\vec{\theta}_{ML}$ is dependent on the validity of the assumptions. We have assumed (i) Gaussian stationary noise, (ii) the LSA (i.e. the presence of high ρ) to be valid, (iii) 'flat priors' and (iv) Γ^{ij} being correctly invertible to Σ^{ij}.

4.3.1   Gaussian noise

Assuming that the noise has a Gaussian shape, is a reasonably good approximation at this point. All the previously described noise sources are inherently connected to randomness. The combined effect of all these tends to produce nearly Gaussian shaped noise. It is however, possible to add non Gaussian terms to describe the noise, which can help to recognise weaker signals present in the data. This will however lack relevance to our analysis as we will only be looking at strong signals as we are limited by the LSA to high SNRs [38, 39].

4.3.2   Signal-to-noise ratio

The main assumption that has to be addressed is the validity of the LSA. This linearisation is, as described in section 4.2, an approximation valid in the presence of high SNR. GWs are detected at SNRs of 8 and larger, but the validity of the Fisher matrix at these SNRs is very uncertain. This is because σ_i falls of as SNR^{-1}, but the real uncertainties do not need to follow this behaviour. The simulations made in [40], clearly indicate this by comparing the Fisher formalism to the, more extensive, Monte Carlo method. Although they only used a waveform up to 1PN order, it is still indicative to know that the Fisher formalism underestimated the uncertainties in the estimation by over a factor of 2 at an SNR of 10. At an SNR of 25 this mismatch disappeared. A more extensive analysis of the SNR-domain in which the Fisher matrix is a decent approximation is done in [41]. Where a quantisation of the mismatch between the waveform in the LSA and the waveform without loss of higher-order terms is derived. This is defined as:

$$|\log r(\vec{\theta})| = \left(\frac{\partial h(\vec{\theta}_{ML})}{\partial \theta^i} \delta\theta_i - \Delta h(\vec{\theta}) | \frac{\partial h(\vec{\theta}_{ML})}{\partial \theta^j} \delta\theta_j - \Delta h(\vec{\theta}) \right) /2, \tag{49}$$

where $\Delta h(\vec{\theta}) = h(\vec{\theta}) - h(\vec{\theta}_{ML})$, $h(\vec{\theta}) = h(\vec{\theta}_{ML}) + \frac{\partial h(\vec{\theta}_{ML})}{\partial \theta^i}\delta\theta^i + ...$, $|\log r(\vec{\theta}, \rho)|$ the quantisation of mismatch and $|.|$ the norm associated with an inner product. The derivative term $\frac{\partial h(\vec{\theta}_{ML})}{\partial \theta^i}\delta\theta_i$ is the deviation from $h(\vec{\theta}_{ML})$ used to derive the Fisher matrix and $\Delta h(\vec{\theta})$ the deviation from $h(\vec{\theta}_{ML})$ in a Taylor expansion in which higher-order terms are not neglected.

Subsequently, a cumulative distribution function for the mismatch $|\log r|$ is calculated on the 1σ curface of the multivariate Gaussian given by the Fisher matrix.
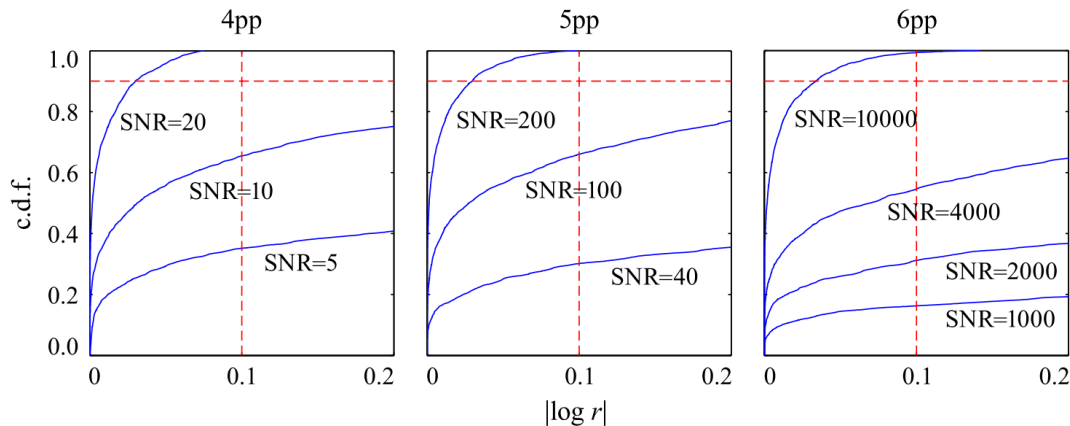

Figure 11: Cumulative distribution for $|\log r|$ on a surface as described above for the 4, 5 and 6 parameter case and for multiple ρ-values. Evaluated in the case of $m_1 = m_2 = 10 M_\odot$, a restricted waveform up to 2PN and a Fisher matrix calculation for the parameters: $(t_{\text{coal}}, \Phi_{\text{coal}}, \mathcal{M}_c, \eta)$, with the 3PN spin parameter added to the calculation in the 5 parameter case and the 3PN and 4PN spin parameters added in the 6 parameter case. Flat priors were imposed and the strived for c.d.f. is one where 90%[i.e. 0.9 above] of the distribution has a mismatch of maximum 0.1 [i.e. 90% of the points on the surface, calculated in accordance with the Fisher matrix, have a mismatch smaller than the value 0.1] [41].

In contrast with [41], we do not include spin parameters, use a restricted waveform up to 2PN or only add parameters at 3PN or 4PN. This model does however correspond to our model in a general way, which justifies our adoption of its global conclusions.
The first thing we can derive is that in the case of extremely large SNR, the described mismatch stays below 0.1, which means that the LSA 'creates' a self-consistent Fisher matrix. The second thing we can derive is that when more parameters are determined, the SNR needs to enlarge by at least a factor of 10 to validate the use of the LSA.
In the case of the model used in [41], the Fisher matrix becomes self-consistent for SNR$\in$ $[10, 20]$ in the 4 parameter case, for SNR$\in$ $[100, 200]$ in the 5 parameter case and for SNR$\in$ $[4000, 10000]$ in the 6 parameter case. As we will mostly be looking at the 5 parameter case, we will strive for SNRs of at least 100 and take into account that the Fisher matrix certainly underestimates the uncertainties in the estimation below this SNR, as analysed by [40].

4.3.3   Flat priors

As stated in section 4.2, we assume flat priors (i.e. uniformly distributed parameter probability distributions that describe our knowledge of the parameters). This assumption is usually applied in Bayesian Analysis when one wants the priors to have as little influence as possible,

since flat priors result in the likelihood being proportional to the PDF. Hence, choosing flat priors, which have the least amount of impact, can be seen as the safest choice.

4.3.4   Inverse

Determining the inverse of Γ^{ij} is the last step in determining the RMS deviations of the parameters. One obvious situation in which problems arise is when a Fisher matrix is singular and thus by definition does not have an inverse. In the case of numerical simulations it can occur that the Fisher matrix is perceived as singular by the computer due to such large differences between the diagonal elements that the ratio between them approaches floating-precision [42]. This can be solved partly by reducing the differences between the diagonal elements by equating the Fisher matrix for the logarithm of the parameters. So instead of $\mathcal{M}_c$ and η we will be using $e^{\log \mathcal{M}_c}$ and $e^{\log \eta}$ as parameters of our waveform. Still there are situations in which this is not sufficient and Singular Value Decomposition must be applied to calculate a 'pseudo-inverse'. We have chosen not to quote results obtained in this way, thus for further information regarding SVD, we refer to [42].

5   A NETWORK OF DETECTORS

To describe ET using the Fisher formalism, we need a Fisher formalism valid for a network of V-shaped detectors. Let us first have a look at the necessary modifications to the waveform.

5.1   Wavefrom

According to [33], the antenna pattern functions, described in Eqs. (6) and (7) for an L-shaped interferometer (90° angle between its arms) are a factor $\sqrt{3}/2$ smaller for a V-shaped interferometer (60° angle between its arms):[15]

$$F_+^V(\theta, \phi, \psi) = \frac{\sqrt{3}}{2} F_+^L(\theta, \phi, \psi), \tag{50}$$

$$F_\times^V(\theta, \phi, \psi) = \frac{\sqrt{3}}{2} F_\times^L(\theta, \phi, \psi). \tag{51}$$

This describes the antenna pattern function of one V-shape. The other two V-shaped interferometers present in ET are described by the transformation $\phi \to \phi \pm 2\pi/3$. This results in the following antenna pattern functions for interferometers 2 and 3:

$$F_{+,\times}^2(\theta, \phi, \psi) = F_{+,\times}^1(\theta, \phi + 2\pi/3, \psi), \tag{52}$$

$$F_{+,\times}^3(\theta, \phi, \psi) = F_{+,\times}^1(\theta, \phi - 2\pi/3, \psi). \tag{53}$$

where $F_{+,\times}^1$ is equal to $F_{+,\times}^V$ from Eqs. (50) and (51).

5.2   Signal-to-noise ratio

We now have all the tools we need to calculate the SNR for each interferometer present in ET: the modified waveforms and the PSD as described in section 3.5. To combine the SNRs, the following equation can be used [33]:

$$SNR_{tot} = \sqrt{SNR_1^2 + SNR_2^2 + SNR_3^2}, \tag{54}$$

where SNR_n, with $n = 1, 2, 3$, denotes the SNR of interferometer $1, 2, 3$ and SNR_{tot} denotes the SNR of ET. The $\frac{\sqrt{3}}{2}$ term that is added to the antenna pattern functions in section 4.1, decreases the SNR of one detector, according to Eq. (34), with an equal factor of $\frac{\sqrt{3}}{2}$. However, because of Eq. (54), this results, in the case of three identical detectors and an equal sky location and orientation of the binary for all three detectors $\{\theta, \phi, \psi, \iota\} = 0$, in an overall increase of a factor of $\frac{3}{2}$ in SNR for three V-shaped detectors with arm lengths X compared to one L-shaped detector with equal arm lengths X [33]. Following the same argument, three identical L-shaped detectors would have an overall increase in SNR of maximally a factor $\sqrt{3}$, relative to one L-shaped detector.

---

[15]From now on, we view the two interferometers present in one V-shape as one interferometer. The combined sensitivity of the LFI and HFI of ET is visualised in figure 9.

5.3   Fisher matrix

After the modification, discussed in section 5.1, to the waveform, the Fisher matrix can be calculated for all three V-shaped detectors separately. To combine the three matrices, we need to have a look at Eq. (45). We can combine the probability distributions of the three detectors by multiplying them [43]:

$$p(\delta\vec{\theta}) \propto p_1(\delta\vec{\theta})p_2(\delta\vec{\theta})p_3(\delta\vec{\theta}) \propto e^{-\frac{1}{2}(\Gamma_1^{ij}+\Gamma_2^{ij}+\Gamma_3^{ij})\delta\theta^i\delta\theta^j} \propto e^{-\frac{1}{2}(\Gamma_{tot}^{ij})\delta\theta^i\delta\theta^j}. \tag{55}$$

This leads us to conclude that, to combine the three interferometers, we need to add the separately calculated Fisher matrices:

$$\Gamma_{tot}^{ij} = \Gamma_1^{ij} + \Gamma_2^{ij} + \Gamma_3^{ij}, \tag{56}$$

where Γ_{tot}^{ij} indicates the Fisher matrix of ET and Γ_n^{ij} with $n = 1, 2, 3$ the Fisher matrices of the separate interferometers.

6   TESTS OF GENERAL RELATIVITY

As coalescences of BBHs and BNSs are ideal subjects for tests of the strong-field regime of GR, multiple tests have been devised and executed for the recently detected GW signals. One of these checks for possible deviations in the PN coefficients by studying the phase evolution related to the inspiral of a binary system.[16] In this chapter we will (i) briefly summarise how this test is done in practice, (ii) present our results related to the Fisher matrix, (iii) analyse the results derived by [5, 6], (iv) compare our Fisher matrix formalism to these tests and (v) evaluate to what extent these tests can be enhanced by use of ET.

6.1   Parameterised tests of the PN formalism

As there are, at this time, no high-accuracy predictions for IMR waveforms in alternative theories of gravity, there is no possibility in testing GR by comparing its predictions of the waveforms arising from binary coalescence to other theories. What is possible though, is investigating to what degree the given GW data is described by waveforms that have been derived from GR, by constraining deviations from Einstein's theory [5].
In the case of [5, 6] this has been done with the waveform model IMRPhenomPv2 in the former case and PhenomPNRT in the latter case, which describe the whole IMR regime for BBHs and only the inspiral regime for BNSs respectively. The phase of these waveform models is described by a number of coefficients $\{p_n\}$: (i) during early-inspiral by the, from section 2.4, familiar PN coefficients $\{\alpha_0, ..., \alpha_7\}$ and $\{\alpha_{5l}, \alpha_{6l}\}$ and (ii) in the case of BBHs by a set of other coefficients during late-inspiral, merger and ringdown.[17] By now introducing the following parameterised deformations to these coefficients:

$$p_n \rightarrow (1 + \delta\hat{p}_n)\, p_n, \tag{57}$$

the waveform is given the freedom to deviate from the by GR defined values of these co-efficients, with $\delta\hat{p}_n$ being the relative deviation testing parameter. When this waveform, which includes the testing parameters, is matched to GW data, all the parameters (masses, spins, sky position, orientation, distance, coalescence time, coalescence phase and testing parameters) are estimated and, in the case of GR being confirmed for that detection, all testing parameters should have the value $\delta\hat{p}_n = 0$ supported by their PDFs. In the case that deviations from zero are present, these do not necessarily reflect the coefficient values of the correct theory. Determining coefficients for 'the correct theory' would have to be done through the construction of a new IMR model for that particular theory [6]. So this is no method for determining a new theory of gravity. This does however reflect to what extent the IMR waveform, derived from GR, is applicable to that specific GW detection. Note that the testing parameters do not receive the freedom to deviate all at a time. One parameter is allowed to vary freely, while the others are fixed to zero. This allows us to answer the more specific question: "does one or more of the testing parameters vary from zero?" in stead of the more general question: "do all testing parameters vary from zero?", and it helps to reduce statistical errors, as these will be smaller for the estimation of less parameters [44, 45].[18]

---

[16]The GW amplitude is not analysed, [1] explains why.

[17]We refer to [5, 6] for exact details on these coefficients as we confine ourselves to early-inspiral.

[18]Just like in the Fisher matrix case, see section 4.3.2.

Note that not all coefficients have a measurable testing parameter because of their degeneracy with another parameter. α_5 for example, is completely degenerate with the coalescence phase. Note too, that $\delta\hat{\alpha}_1$ represents an absolute instead of a relative deviation, due to $\alpha_1 = 0$ [6].

The accuracy to which the PDFs are determined is, of course, dependent on the SNR. The higher the SNR, the stronger the signal and the more accurately a waveform can be matched to a signal. However, strong signals in GW detectors are often caused by BBHs with a total mass larger than $50M_\odot$ [5], that would, after a similar calculation as in section 3.4 and considering the BHs to be of equal mass, be in the observation band of the current AdLIGO detector with $f_{cutoff} = 20$ Hz, for a bit more than a second and would have an $f_{ISCO} \approx 87$ Hz.[19] While BBHs with a total mass of $20M_\odot$ would have a lower SNR but be detectable, after a similar calculation and considering again that the components are of equal mass, for four times as long and would have $f_{ISCO} \approx 219$ Hz. As ground based GW detectors experience their peak sensitivity at frequencies in the bandwidth $[100, 300]$ Hz (see section 3.3), the signal of a smaller mass BBH can still be more informative and thus be favourable, even though it has a smaller SNR. An ideal situation is of course the detection of a source that has a high SNR and which is in the detection band for a long period of time.

As analyses of separate events are dominated by statistical uncertainties due to the presence of detector noise, combining events to reduce these statistical errors can be useful in determining the testing parameters [5]. Combining events with our Fisher analysis will be executed in Chapter 7 and will be discussed in the outlook.

6.2   Results

By implementing the testing parameters into the Fisher formalism using Mathematica [46] we are able to estimate a measure the measurability of these testing parameters for future 3G detectors. The Fisher formalism is obviously not a suitable method for determining the expectation value of parameters, as is clarified in chapter 4. It is however useful to determine an indication of the measurability of parameters. Therefore, we will only look at the spread in the PDFs related to the testing parameters. Because of the uncertainties associated with the Fisher formalism, we will be focusing at orders of magnitude. A more in-depth analysis is needed to achieve more accurate results.

We execute the analysis for AdLIGO at a downgraded sensitivity and ET at design sensitivity, with help of the PSD curves from section 3.5. All BBHs analysed in [5] and the BNS analysed in [6] have been subjected to a Fisher analysis. Our analysis consists of adding the testing parameters, as described in section 6.1, to our early-inspiral waveform model. By now evaluating the Fisher matrix for each testing parameter in turn, in combination with the parameters $\{t_{\text{coal}}, \Phi_{\text{coal}}, \log\mathcal{M}_c, \log\eta\}$, we are able to derive the spread in the PDFs related to the testing parameters. This makes it applicable to the 5 parameter case, described in section 4.3.2, which requires a high SNR (somewhere in the range SNR$\in [100, 200]$ the Fisher matrix becomes self-consistent). At a lower SNR we can expect an underestimation of the spread in the parameters. Let us now talk about the relevant decisions we have made during this analysis.

---

[19]In the case of BBH mergers, the IMRPhenomPv2 would be able to analyse the signal up to higher frequencies, but this does equally apply to smaller mass BBHs.

- Our waveform model does not describe anything other than early-inspiral. This makes it computational and understandable, but will inevitably result in a loss of information. Especially in the case of BBHs, with a limited number of inspiral wave cyles inside the detection band, uncertainties will be larger for our model due to loss of information. To counter this loss of information we evaluate binaries of smaller mass, as these are favourable due to their longer inspiral, as described in section 6.1. That is why we will discuss a lower mass BBH [GW151226] and the BNS [GW170817] below. The other analyses of the BBHs are presented in the appendix. Our waveform model does also neglect tidal effects and spins. We expect these simplifications to be negligible compared to the inherent errors associated with the Fisher formalism. In chapter 7 we will analyse the detectability of the tidal effects for various detectors.

- To reasonably compare our Fisher formalism for a single detector at AdLIGO design sensitivity to the more extensive analysis done by [5, 6], which is based on real data collected by the AdLIGO and AdVIRGO detectors not being at design sensitivity, we normalise our SNR to equal the SNR associated with the actual detections. This normalisation includes (i) a downgrade in sensitivity, as we are using the PSD for AdLIGO at design sensitivity, (ii) an upgrade in sensitivity, as we are evaluating the detection of a GW with only one detector in contrast with the network of detectors used in the extensive analysis and (iii) a factor that re-scales the impact of the non-perfect location of the binary on the SNR. One could try to model a combination of AdLIGO and AdVIRGO at the exact sensitivity at which they were at the time of measurement, including sky locations etc.. But because of the inherent errors associated with the Fisher formalism, we expect such models to be unnecessarily complex and our approximation to be sufficient.

- As GW sources are not likely to be perfectly located and oriented in the case of detection, we average over the sky position and orientation by multiplying our SNR with a factor of $\frac{2}{5}$ in the case of ET [12]. In the case of AdLIGO the non-perfect location is incorporated in the re-scaling of the SNR.

- The masses used are source frame masses (i.e. the actual masses of the binary) as the measured masses have been divided by a factor of $(1 + z)$, with z being the redshift [47].

- Because of the usage of 90% upper bounds by [5, 6], we do the same and convert our 1σ (i.e. 68%) bounds to 90% upper bounds.

- As we are dealing with relative deviations, a value of $|\Delta\delta\hat{\alpha}_n| = 1$ resembles a 90% spread of the PDF as large as the associated value of α_n. From this point up, the 90% upper bounds become relatively uninformative, as only unlikely large deviations of the testing parameters from 0 can be deemed measurable. But, because of ET having values $|\Delta\delta\hat{\alpha}_n| < 1$ for all PN orders, for completeness, we will include the probably uninformative values of $|\Delta\delta\hat{\alpha}_n|$ for Fisher-AdLIGO and the extensive analysis since one could argue that uninformative values are equally instructive as informative values. They namely tell us that a deviation is probably unmeasurable for that specific detector, which can also be deemed to be a useful result when one is comparing detectors.

- Due to problems related to inverting the Fisher matrix to derive the uncertainties in the testing parameters, we choose not to visualise the uncertainties related to the PDFs of the testing parameters obtained by SVD, see section 4.3.4, as they are derived with help of pseudo-inverses. This is the reason for the regular absence of values at 2PN and $3PN^{(l)}$. But even in the cases in which 2PN and $3PN^{(l)}$ have been determined, we do not fully understand their behaviour, especially as described by Fisher-AdLIGO. However, as the actual measurements estimate $|\Delta\delta\hat{\alpha}_n| > 1$ at $n = 4, 6l$ (i.e. bounds on the testing parameters are probably uninformative), we will not give to much attention to these PN orders.
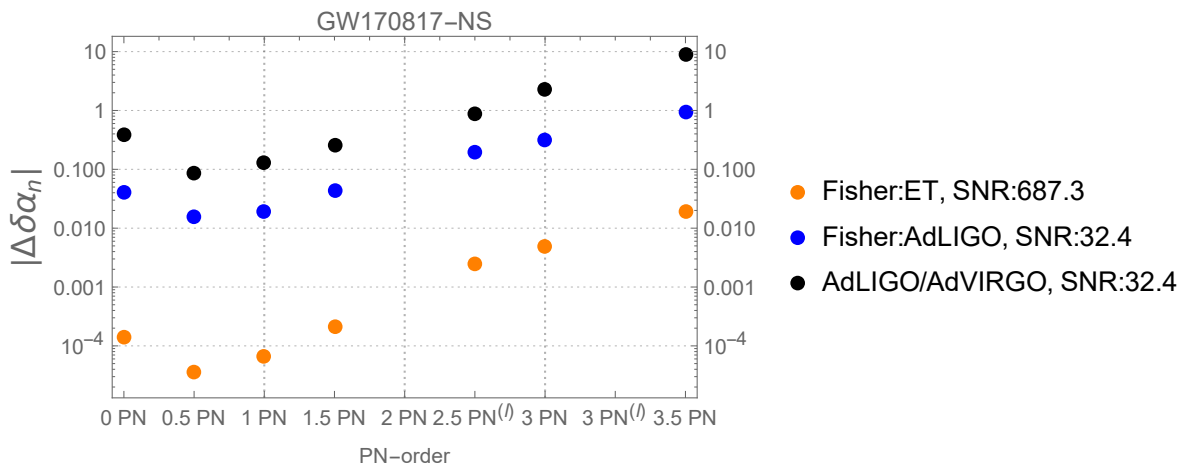
Let us now visualise the discussed data.

Figure 12: 90% upper bounds $|\delta\hat{\alpha}_n|$ on the absolute magnitude of the testing parameters for GW170817 ($m_1 = 1.5M_\odot, m_2 = 1.3M_\odot, d = 40$ Mpc) [2] determined by: (i) the Fisher matrix adjusted to resemble ET at design sensitivity, (ii) the Fisher matrix based on the AdLIGO design sensitivity, but re-scaled to resemble the (iii) analysis based on the actual AdLIGO/AdVIRGO detection, as described in [6], using the PhenomPNRT waveform. Note that these are relative deviations (except for the 0.5PN term).
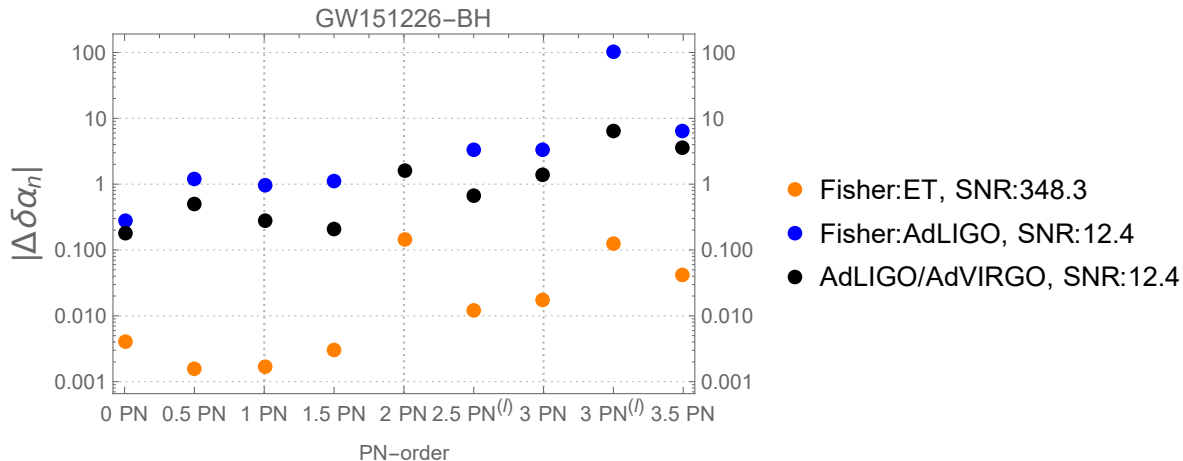
Figure 13: 90% upper bounds $|\delta\hat\alpha_n|$ on the absolute magnitude of the testing parameters for GW151226 ($m_1 = 13.7M_\odot, m_2 = 7.7M_\odot, d = 450$ Mpc) [48] determined by: (i) the Fisher matrix adjusted to resemble ET at design sensitivity, (ii) the Fisher matrix based on the AdLIGO design sensitivity, but re-scaled to resemble the (iii) analysis based on the actual AdLIGO/AdVIRGO detection, as described in [5], using the IMRPhenomPv2 waveform. Note that these are relative deviations (except for the 0.5PN term).

6.3   Existing measurements

We will now first evaluate the data as derived from the extensive analyses done by [5, 6] (i.e. the black data). The values of $|\delta\hat\alpha_n|$ (i.e. the spread in the testing parameters) are lower at lower PN-orders (0-1.5PN) relative to higher PN-orders (2-3.5PN) in all cases (figures 12 and 13 and the figures in the appendix). This indicates that the deviations from GR are best measurable at low PN-orders. At higher PN-orders the values $|\delta\hat\alpha_n|$ are almost always larger than one, which indicates that these can be deemed to be uninformative, unless of course GR, all of a sudden, happens to be off by miles. What we, obviously, do not expect. If we compare the figures 12 and 13 to the figures in the appendix, we can also derive that the tightest constrains on GR are, as expected and explained in section 5.1, at high SNRs and for sources that spend the longest amount of time in the detection band (i.e. lower mass sources).

6.4   Fisher-AdLIGO versus existing measurements

We will now compare the spread in the PDFs for the testing parameters derived from (i) our Fisher matrix in the case of AdLIGO (i.e. the blue data) to (ii) the extensive analyses made by [5, 6] (i.e. the black data). Our goal is to determine to what extent the Fisher formalism is capable of reproducing these data-based results for low SNRs and to determine what limits our formalism in deriving the same results as [5, 6].

To summarise: the maximum-likelihood values derived in the measurements are used in the Fisher matrices and SNRs are matched to, first, modify the AdLIGO PSD at design sensitivity to be of similar shape as the AdLIGO PSD at time of measurement, second, equalise the influence of the location and orientation of the source on the SNRs and third, compensate

the difference in the amount of detectors used. The waveform used in [6] in the BNS case is PhenomPNRT. Because of the fact that this model does not describe the waveform in the merger and post-merger regimes, we are helped in comparing our simplified analysis to a more extensive one. The wavefrom used in [5], in the BBH case is IMRPhenomPv2, which does describe the waveform during inspiral, merger and ringdown. A lot less information is lost with the use of IMR waveforms that will inevitably lead to smaller uncertainties in the estimation of the testing parameters in the case of [5] relative to our own Fisher calculations. There is however, when using the Fisher matrix at low SNRs, an underestimation in uncertainties to be expected.

6.4.1   Binary neutron star

If we now have a look at figure 12, we are able to see that the Fisher formalism expects, just like the actual measurement, a better measurability of the testing parameters at lower PN-orders and a clear similar trend is visible in the data. The Fisher matrix does however approximate the values of $|\delta\hat{\alpha}_n|$ to be smaller by an approximately constant factor of 10 relative to the actual measurement. Because of this underestimation, the fisher matrix expects all PN-orders to be reasonably informative [i.e. $|\Delta\delta\hat{\alpha}_n| < 1$]. This is however not the case in reality, according to the analysis made by [6]. Because of the use of similar waveforms, our application of the source parameters as derived by these same actual measurements, our levelling of the SNRs, and the prior knowledge that the Fisher matrix underestimates the uncertainties at low SNRs, we deem ourselves justified in stating that the major part of the underestimation is due to the Fisher formalism itself.

6.4.2   Binary black hole

Now lets have a look at figure 13 and the figures visualised in the appendix. Again we are able to see that the Fisher formalism estimates that the testing parameters are better measurable at lower PN-orders, just like the actual measurement, and we are able to see a similar trend. This trend is however not as 'spot on' as in the BNS case, since we are dealing with over- and under-estimations in this case, opposite to just underestimation in the BNS case. This can be explained by the loss of information due to our waveform, which only describes early-inspiral. The absence of a description for the waveform in the merger and post-merger/ringdown regimes in the case of our Fisher formalism inevitably leads to an increase in $|\delta\hat{\alpha}_n|$. Such an increase apparently, that it outdoes the decrease in uncertainty associated with the Fisher matrix at low SNRs. In the case of BBH estimations using the Fisher matrix and an early-inspiral waveform at SNRs this low, a balance between (i) the absence of a description of merger and ringdown increasing the uncertainty and (ii) the Fisher-matrix underestimating the uncertainty, seems to be induced. When looking at the appendix we see that the Fisher estimated values of $|\Delta\delta\hat{\alpha}_n|$ fit worse to the extensive analysis in the case of (i) even heavier mass binaries and lower SNRs. This is to be expected due to the even greater loss of information in the case of even shorter inspiral periods related to larger masses and the even greater underestimations made by the Fisher matrix for even lower SNRs. These two sources of error seem to keep each other in balance as they do not

create massive deviations in the error bounds on the testing parameters in the case of Fisher, relative to the actual measurement. The deviations are, as in the BNS case, no larger than an order of magnitude. They do however destroy the trend set by the extensive analysis, as is best seen in figure 21 (GW170104).

6.4.3   Conclusions

First, we can conclude that our Fisher formalism is primarily limited in reproducing the actual measurements by (i) low SNRs in BNS and BBH cases and by (ii) our used waveform in the case of BBHs. Longer inspirals and higher SNRs are circumstances in which our Fisher formalism will reproduce the actual measurements with higher accuracy and thus be more reliable. These limiting factors leads to an error of approximately one order of magnitude in the AdLIGO case as discussed above, which is not great but as expected from Fisher matrix analyses at low SNRs. The Fisher formalism at low SNRs and for sources of short duration should be seen as an indication of the measurability of parameters. No hard limits on the measurability by a detector can be defined, but it does give us an indication.

Second, we can conclude from figure 13 and the other analyses visualised in the figures in the appendix that: in the case of BBHs, using only an early-inspiral waveform and with use of detectors at current SNRs, no useful bounds on the testing parameters can be determined that would help us actually test GR, according to the Fisher matrix. And as the Fisher matrix has a tendency to underestimate uncertainties, we expect it to be very unlikely that any relevant bounds can be determined by modern day detectors using an early-inspiral waveform. With use of an IMR waveform, meaningful bounds can be derived up to 1.5PN, as discussed in section 6.3.
We will now be evaluating to what extent ET will be capable of measuring deviations from GR.

6.5   Fisher-ET versus existing measurements

We will now compare the spread in the PDFs for the testing parameters derived from (i) our Fisher matrix in the case of ET (i.e. the orange data) to (ii) the extensive analyses done by [5, 6] (i.e. the black data), with the behavioural characteristics of the Fisher matrix, as derived in section 6.4, in the back of our minds. Our goal is to determine to what extent the measurability of the testing parameters will be enhanced by ET. An increase in measurability (i.e. decrease in the parameters $|\Delta\delta\hat{\alpha}_n|$) is of course expected for ET. This is generally due to (i) the SNR being larger than 200, that results according to section 4.2 in a decrease in the spread, and (ii) the lower value of f_{cutoff} that will result in signals being detectable for longer periods of time and an increase in information accordingly, see section 6.1. We assume an $f_{cutoff} = 3$ Hz, which is still a reasonably conservative estimation. Note that the lower value of f_{cutoff} will specifically increase the detectability of the earliest parts of inspiral. As low PN coefficients are more important than high PN coefficients for the earliest parts of inspiral, we expect these to benefit the most from this decrease in f_{cutoff}, i.e. we expect $|\Delta\delta\hat{\alpha}_n|$ to decrease more at low PN values than at higher PN values in the case of ET.

For ET, a Fisher model is constructed in the same manner as was done for AdLIGO in section 6.4, with modifications according to chapter 5. I.e. we use the same maximum-likelihood values and same early-inspiral waveform, but use the PSD for ET at design sensitivity and generalise our Fisher model to resemble a combination of three detectors. As described in section 6.2 we average over sky position.

We expect a Fisher formalism based on ET to be a better representation of actual measurements than a Fisher formalism based on AdLIGO. This is partly due to the higher SNRs that are expected for ET, which make the Fisher formalism self consistent for the 5 parameter case, as discussed in section 4.3.2, and this is partly due to the lower value of f_{cutoff}. This improvement from $f_{cutoff} = 20$ Hz to $f_{cutoff} = 3$ Hz compensates, to some extent, the experienced deviation of our Fisher formalism in the BBH case due to neglecting the merger and ringdown in our waveform, as discussed in section 6.4. With a lower value of f_{cutoff}, less information will be lost in the inspiral frequency domain, as there are more cycles of inspiral during which the parameters can be determined. This will compensate the absence of information on the merger and ringdown in our Fisher model, to some extent. Because of ET not being build yet, we can not directly compare our results to actual measurements, but according to the above argument we expect results that are at least as accurate as the results achieved by our Fisher model for AdLIGO.

6.5.1   Binary neutron star

If we now have a look at figure 12, we see that in the case of ET a similar trend is visible as in the actual measurement, only now all values of $|\Delta\delta\hat{\alpha}_n|$ are a factor $[10^2, 10^4]$ smaller. Especially the testing parameters at lower PN-orders benefit from the use of ET, as explained above. ET is capable of defining bounds smaller than 1, on all the testing parameters.

6.5.2   Binary black hole

Let us now have a look at figure 13 and the figures visualised in the appendix. ET follows, again, a similar trend as the actual measurement, but does not do this as accurately in the BBH cases as in the BNS case. The values of $|\Delta\delta\hat{\alpha}_n|$ decrease, in the case of small mass BBHs, with a factor of $[10^1, 10^3]$ (GW170608, GW151226) and in the case of larger mass BBHs (GW150914, GW170814, GW170104) with a factor of $[10^1, 10^2]$. The testing parameters at lower PN-orders benefit, just like in the BNS case, the most. No values for $|\Delta\delta\hat{\alpha}_n|$ are larger than 1, which means that Fisher is capable of defining informative spreads for all PSDs of the testing parameters.

6.5.3   Conclusions

We can conclude from this analysis that ET will inevitably lead to significantly tighter bounds on the testing parameters when compared to 2G detectors, especially for lower PN orders. 2G detectors are able to define bounds on the testing parameters, in the range of $[10,100]\%$ for lower PN orders and $[100, \rightarrow\rangle\%$ for higher PN orders, when detecting long inspiralling, high SNR binaries, and, in the case of short signal, low SNR binaries, bounds in the range of $[10, \rightarrow\rangle\%$ for lower PN orders and $[100, \rightarrow\rangle\%$ for higher PN orders. While ET probably, if

we make conservative estimations, will lead to bounds in the range of [0.1,1]% for lower PN orders and [1,10]% for higher PN orders, when detecting long inspiralling, high SNR binaries, and, in the case of short signal, low SNR binaries, to bounds in the range of [0.1,10]% for lower PN orders and [1,100]% for higher PN orders.

Because of the significantly increased detection rates expected for ET, see section 3.5, even tighter bounds will be derived from the combination of multiple detections.

Note too that, when using IMR waveforms, the bounds on the testing parameters are probably even tighter than the ones we determined as the inspiral-waveform inevitably experiences a loss of information by not describing the full waveform. We can conclude that Einstein's theory will be properly put to the test by ET.

The certainty of these claims stands or falls with the Fisher matrix. As we expect our Fisher formalism to have smaller deviations from actual measurements at higher SNRs and for sources that are detectable for longer timescales, we expect these bounds on $|\Delta\delta\hat{\alpha}_n|$ to be correct within an order of magnitude.

7   TESTS OF NEUTRON STAR EQUATION OF STATE

Besides testing the strong-field regime of GR, the detection of coalescing BNSs with GW detectors can be used to gain knowledge of the neutron star equation of state EOS, about which we know very little still.[20] In this chapter we will (i) summarise how the EOS enters our waveform model, (ii) discuss an extensive analysis: [7], on which our analysis is based, (iii) discuss our own analysis, (iv) compare our results in the case of AdLIGO with the results of the extensive analysis and (v) discuss our results in the case of ET.

7.1   EOS in our waveform model

The EOS enters a GW signal in the following three ways: (i) tidal deformations, (ii) early termination of the waveform due to contact between the NSs and (iii) the quadrupole-monopole effect. This last effect is irrelevant to our analysis as it is dependent on spin, which is not included in this paper. An allowed simplification, according to [49], since spins are expected to be small for BNSs.[21] We will now discuss (i) and (ii) as we do implement those into our Fisher analysis. We will be following earlier work: [7].

7.1.1   Tidal deformations

The primary way the EOS enters the GW signal is through tidal deformations. During the last stages of inspiral ($f > 400$ Hz) a tidal field $\mathcal{E}_{ij}$ in one NS induces a quadrupole moment Q_{ij} in the other. The strength of this quadrupole moment is dependent on the EOS through the tidal deformability $\lambda(EOS; m)$ of the NS in which a quadrupole moment is induced. This happens according to the following expression in the, in section 2.4 described, adiabatic approximation:

$$Q_{ij}^{(2)} = -\lambda^{(2)}(EOS; m)\mathcal{E}_{ij}^{(1)}, \tag{58}$$

with the numbers denoting that the induced quadrupole moment in a NS is determined by its own tidal deformability and the tidal field of the other NS, with $\lambda(EOS; m)$ denoting that the tidal deformability is dependent on the mass through the EOS, according to the following equation:

$$\lambda(m) = \frac{2}{3}k_2(m)R^5(m), \tag{59}$$

with k_2 being the second Love number and $R(m)$ the neutron star radius.
The induced quadrupole moments in the two NSs deform them and effect their orbital motions and the GWs they produce. The EOS can in turn be derived from the detected GWs.
The EOSs we review are plotted in figure (14).

---

[20]NSBH coalescence can also be evaluated, but in this paper we will focus on the BNS case. The formalism we use can be applied as it is to NSBHs as well. We leave this to future research.

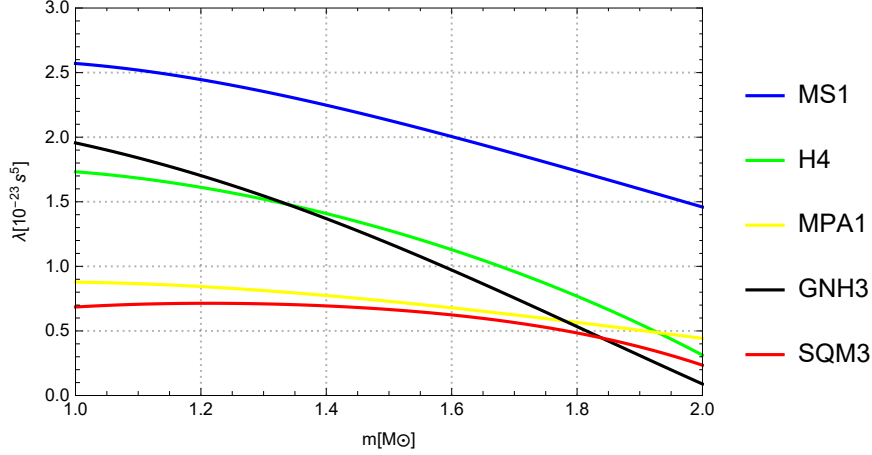[21]For more information on the quadrupole-monopole effect, see [7].

Figure 14: The various EOSs used in this paper, with on the horizontal axis the mass of a NS in solar masses and on the vertical axis the tidal deformability λ, with MS1 being the stiffest and SQM3 the softest EOS [4].

Note that a stiff EOS has the largest tidal deformability and a soft EOS the smallest tidal deformability.

These tidal effects enter the GW phase at 5PN order and are determined up to 7.5PN order by [50]. They can be added linearly to the existing phase up to 3.5PN order, as presented in section 2.4, like: $(\Psi_{NS}(f) = \Psi(f) + \Psi_{tidal}(f))$, with $\Psi_{tidal}(f)$ being, according to [50]:

$$
\begin{aligned}
\Psi_{\text{tidal}}\left(f\right) =& \frac{3}{128\eta}v^{-5}\sum_{A=1}^{2}\frac{\lambda_A}{M^5 X_A}\left[-24\left(12-11X_A\right)v^{10}+\frac{5}{28}\left(3179-919X_A-2286X_A^2+260X_A^3\right)v^{12}\right.\\
&+24\pi\left(12-11X_A\right)v^{13}-24\left(\frac{39927845}{508032}-\frac{480043345}{9144576}X_A+\frac{9860575}{127008}X_A^2\right.\\
&\left.-\frac{421821905}{2286144}X_A^3+\frac{4359700}{35721}X_A^4-\frac{10578445}{285768}X_A^5\right)v^{14}\\
&\left.+\frac{\pi}{28}\left(27719-22127X_A+7022X_A^2-10232X_A^3\right)v^{15}\right],
\end{aligned}
$$
(60)

with $v = (\pi M f)^{1/3}$ as in section 2.4, $X_A = m_A/M$, $\lambda_A = \lambda(m_A)$ and $A = 1,2$. Note that higher-order multipoles have been neglected as they are expected to give negligibly small corrections to $\Psi_{tidal}(f)$ and that a couple of functions at 7PN order have been neglected because of the same reason [7, 50]. Although tidal effects enter the phase at 5PN, they can still be deemed measurable by 2G detectors because of the large prefactor $\lambda/M^5 \propto (R/M)^5 \sim 10^2 - 10^5$.[22]

As we did not include higher-order contributions to the amplitude in deriving Eq. (15), we will also not add higher-order contributions to the amplitude here. This is in line with [7].

---

[22]In the case of NSs in the approximate ranges: $R \in [7.5, 15]$ km and $m \in [1,2]M_\odot$

7.1.2 Early termination of the waveform at contact

Up until now we have used f_{ISCO} as the upper cutoff frequency at which the early-inspiral waveform is no longer a decent approximation, as described in section 2.3. In the case of BNSs there is however the possibility that they already 'touch' at frequencies lower than f_{ISCO} at which the waveform would already breakdown. This $f_{contact}$ is determined with help of Kepler's third law and is given by:

$$f_{contact} = \frac{1}{\pi}\left(\frac{M}{(R(m_1) + R(m_2))^3}\right)^{1/2}. \tag{61}$$

In order to compute the radii $R(m_1)$ and $R(m_2)$ necessary to derive $f_{contact}$, we can use an equation for the compactness $\mathcal{C}$ [7]:

$$\mathcal{C} = 0.371 - 3.91 \times 10^{-2} \ln\frac{\lambda}{m^5} + 1.056 \times 10^{-3}\left(\ln\frac{\lambda}{m^5}\right)^2, \tag{62}$$

which is an equation not only valid for NSs, but universally valid and derived through a numerical fit.

After deriving $\mathcal{C}$ for a particular λ, we can make use of the fact that the radius R, compactness $\mathcal{C}$ and mass m are related through: $R = m/\mathcal{C}$ to arrive at the required radii and $f_{contact}$. Following [7], we impose that the lower frequency of the two corresponds to f_{cutoff}:

$$f_{upper} = min\{f_{ISCO}, f_{contact}\}. \tag{63}$$

Especially for low mass NSs and stiff EOSs, $f_{contact}$ can be significantly smaller than f_{ISCO}. For an overview on the dependence of $f_{contact}$ on masses and EOSs and on when it becomes smaller than f_{ISCO}, see figure 3 in [7].

7.2 Extensive analysis

We will now first compare our results derived using the Fisher matrix for AdLIGO to a more extensive analysis, done by [7] for AdLIGO/AdVIRGO, to, thereafter, analyse to what extent ET improves on the results obtained with these 2G detectors.

[7] carried out two analyses based on Bayesian methods, from which we took one and applied it to our Fisher formalism. We will only discuss the copied Bayesian analysis method: 'parameter estimation'. We will now first summarise the parts of their work that are relevant to us.

This 'parameter estimation' analysis is not based on real BNS GW detections. Instead BNS signals based on different possible EOSs are 'injected' into simulated detector noise, which is stationary, Gaussian and resembles AdLIGO/AdVIRGO at design sensitivity, to then compare millions of waveforms with the simulated data to analyse to what extent EOSs can be distinguished. By combining several of these 'detections', 200 for each EOS to be precise, stronger bounds on the measurability of various EOSs can be derived. But, since the EOS parameter $\lambda(m)$ varies from source to source because of its dependency on the source

its mass, the PDFs for $\lambda(m)$ can not be combined to arrive at stronger bounds. Other parameters need to be identified that do not vary from source to source. Therefore a Taylor expansion of $\lambda(m)$ is evaluated:

$$\lambda(m) \simeq c_0 + c_1 \left(\frac{m - m_0}{M_\odot} \right) + \frac{1}{2} c_2 \left(\frac{m - m_0}{M_\odot} \right)^2, \tag{64}$$

with $m_0 = 1.4 M_\odot$ and c_0, c_1 and c_2 being the EOS coefficients, which will be the same for all sources. PDFs estimated for these coefficients can be combined by multiplying them in a similar manner as done in Eq. (48).

The 'injected' and 'compared' BNS signals in [7] are based on a waveform model similar to our waveform model as derived in chapter 2 and include the same EOS dependent additions to the phase up till 7.5PN order as discussed in section 7.1. On top of this, they include neutron star spins and the spin-dependent quadrupole-monopole effect. They however also do an analysis in which they set all spins to zero. We will focus on this analysis as it resembles our analysis the most.

Note that this analysis is not a method by which the true EOS coefficients can be determined, since these are self-implemented, but only a method by which the spread in the PDFs of the EOS coefficients for various EOSs can be determined, to subsequently determine if various possible EOSs are distinguishable with AdLIGO/AdVIRGO.

Note too that no real sources are used in [7], since at the time of writing no GW sources were detected, let alone BNS GW sources. Till this day AdLIGO/AdVIRGO have detected only two of these [GW170817,GW190425] [51]. As the above described analysis method tries to combine 200 sources, it is currently still a relevant analysis concerning predictions of the future measurability of EOS parameters.

7.2.1   Results

As discussed in the previous section, [7] tries to determine to what extent various EOSs are distinguishable by AdLIGO/AdVIRGO by inserting various simulated BNS sources, which are subjected to three different EOSs, into simulated detector noise to subsequently 'dig' these GW sources out and determine to what extent the EOS coefficients are measurable and distinguishable for the three different EOSs. The EOSs inserted are: a stiff (MS1), moderate (GNH3) and soft (SQM3) EOS, which are visualised in figure 14 and approximated by a Taylor expansion, according to Eq. (64). The PSD for the AdLIGO/AdVIRGO network at design sensitivity is used, with $f_s = 40$ Hz being the lower cutoff frequency. The inserted sources are drawn from a uniform volume in the distance range $D \in [100, 250]$ Mpc, from a uniform mass distribution on $[1, 2]M_\odot$ and spins are set to zero. Sky location and orientation are distributed uniformly on the sphere and ϕ_c is also drawn uniformly from $[0, 2\pi)$. All sources drawn from these distributions have SNRs greater than 8 and smaller than 30. [23] The priors are, just like the inserted sources, assumed to be flat.[24]

For all injected sources, the EOS parameters are determined with their corresponding 95% bounds. Then, as more injected sources are detected and analysed, PDFs are combined to

---

[23]These were deemed realistic values for the detection of NSs. Two years later a BNS was detected with an SNR of 32.4.

[24]For exact information on these, see [7].

derive stronger bounds on the EOS coefficients. c_1 and c_2 are deemed unmeasurable even after the combination of 100 sources. Only the leading order coefficient c_0 can be measured with some accuracy, as can be seen in figure 15.
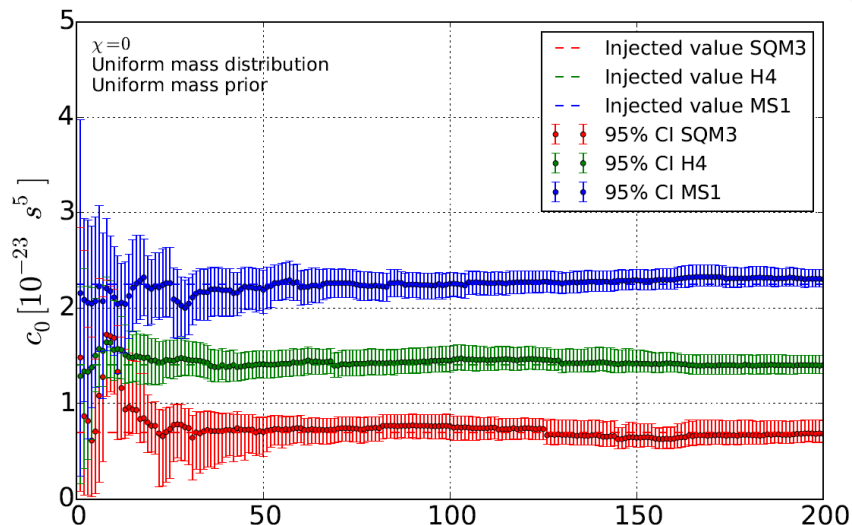

Figure 15: Evolution of the estimated values of c_0 and the 95% bounds in measuring c_0 for injected sources drawn from distributions as described above and detected by AdLIGO/AdVIRGO, for the cases where the injected EOS is: SQM3, H4 or MS1 [7].

In figure 15 can be seen how the PDFs are clearly separated and distinguishable after combining ≈ 50 sources and relative uncertainties of $\approx 10\%$ are reached after ≈ 100 sources have been 'detected' and combined.
Let us now discuss our analysis of the distinguishability of various EOSs using the Fisher matrix.

7.3   Fisher analysis

We will first describe the details of our Fisher analysis in general, to thereafter present our derived results. Our EOS analysis is very similar to our GR test we elaborated on in chapter 6 as it uses the same Fisher formalism for one detector resembling AdLIGO, as described in chapter 4, and the same generalisation to a network of detectors resembling ET, as described in chapter 5.

By implementing the, in section 7.1 discussed, EOS effects into our waveform and by, subsequently, evaluating the Fisher matrix for the parameters $\{t_{\text{coal}}, \Phi_{\text{coal}}, \log \mathcal{M}_c, \log \eta\}$ and, in turn, one of the EOS coefficients, we are able to determine the PDFs for the various EOS coefficients.
With our analysis, we first test to what extent our Fisher analysis is comparable to the extensive analysis done by [7]. We do this to acquire knowledge of the biases of our analysis, to subsequently test how much better ET will be in putting bounds on the EOS coefficients. To make a decent comparison between our analysis and the one discussed in section 7.2 and

to reasonably resemble the future sensitivity of ET, we made some relevant decisions that we will mention now.

- To compare our Fisher analysis to the extensive analysis, we use the PDF of AdLIGO at design sensitivity with $f_{cutoff} = 40$ Hz being the lower cutoff frequency. To reasonably resemble the future sensitivity of ET, we use the PDF of ET at design sensitivity with $f_{cutoff} = 3$ Hz being the lower frequency cutoff.

- We will, similarly to [7], only be looking at the spread of the PDFs of the EOS coefficients and the extent of which EOSs are distinguishable, since parameter estimation is not possible with the Fisher matrix as we implement the values of c_0, c_1 en c_2 ourselves.

- As the analysis executed by [7] draws sources from uniform distributions, we will try to arrive at comparable results by applying our analysis to 'the average source' for the extensive analysis. I.e. we apply our Fisher formalism to: (i) an equal mass case with $m_1 = 1.5 M_\odot$ and $m_2 = 1.5 M_\odot$ as [7] draws from a uniform mass distribution $[1, 2] M_\odot$ and (ii) sources at a distance $D = 202.6$ Mpc as this splits the volume, from which [7] draws its sources, in two. Note that, since all our sources are the same, their PDFs are perfectly combinable, which will lead to a decrease in the evaluated bounds on the EOS parameters by a factor $\sqrt{N}$, see Eq. (48). The PDFs of sources evaluated in [7] are not perfectly combinable due to their different expectation values and spreads. This will lead to a smaller decrease in the evaluated bounds on the EOS parameters after combining multiple sources.

- The PDFs for c_0, c_1 and c_2 are determined, one by one, to make our Fisher formalism applicable to the 5 parameter case, which however requires a high SNR of at least 100. We arrive at an SNR of approximately 18 in the case of AdLIGO, which is a value for which the Fisher matrix will undoubtedly underestimate the spread of the PDFs, see section 4.3.2. This SNR is, however, almost exactly in the middle of the SNR domain of the extensive analysis: SNR$\in [8, 30]$ Mpc. For ET we arrive at an SNR of approximately 165, which should result in the Fisher matrix being self-consistent.

- When comparing our Fisher formalism to the extensive analysis we only evaluate one detector (AdLIGO) as opposed to the network of detectors (AdLIGO/AdVIRGO). This will lead maximally to an SNR that is smaller by a factor of $\sqrt{3}$, as evaluated in section 5.2.

- We average over sky position and orientation by multiplying the SNR with a factor $\frac{2}{5}$ [12] in the case of ET. This averaging is not executed for AdLIGO, first, because the multiplication of the SNR with a factor $\frac{2}{5}$ would lead to a value smaller than 8 and an SNR outside of the realistic domain, as described in [7]. Second, because an SNR this low would also yield even larger Fisher underestimations and third, we already 'downgrade' our SNR, relative to the extensive analysis, by evaluating only one detector as opposed to three. Since we try to resemble a network of three detectors with our analysis of one detector, the neglect of the factor $\frac{2}{5}$, could be seen as a partial compensation for this evaluation of only one detector, which results in a factor $\frac{1}{\sqrt{3}}$.

- We assume flat priors just like the extensive analysis.

- We execute our analysis for the five EOSs visualised in figure 14. Three of these (SQM3, H4 and MS1) have also been reviewed in [7]. The other two (GNH3 and MPA1) have been added to review the possibility of distinguishing between similar, not only between hard, moderate and soft EOSs.

- Because of [7] using 95% bounds, we do the same and convert our 1σ [i.e. 68%] bounds to 95% bounds.

- Following the same arguments as applied in section 4.3.4, we will use $e^{\log c_n}$ in stead of c_n, to increase the quality of the inverse.

This analysis, of course, does not perfectly resemble the extensive analysis or reality. In the light of the inherent errors associated with the Fisher formalism, we do however assume these assumptions to be sufficient when focusing solely on orders of magnitude, the distinguishability of the various EOSs and when reviewing hundreds of GW sources, resulting in our 'average source approximation' to be more reasonable.

7.4   Fisher-AdLIGO versus extensive analysis

In the case of our Fisher analysis applied to AdLIGO, c_1 and c_2 are deemed unmeasurable, which is in correspondence with the results obtained by [7]. This is visualised in figure 24 and figure 26 in the appendix, in which can be seen how the various values of c_1 and c_2 associated with various EOSs are indistinguishable in the case of AdLIGO. Let us now visualise the c_0 case in which various EOSs are deemed distinguishable according to our Fisher formalism.
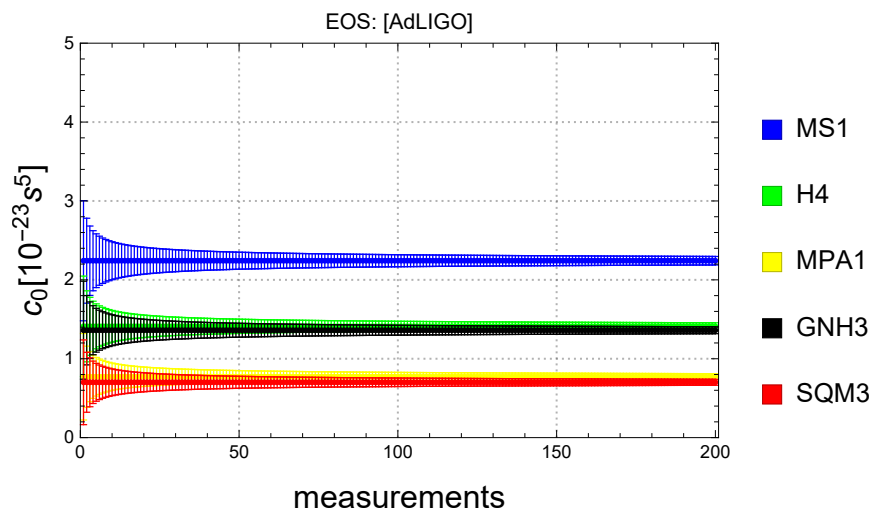

Figure 16: Evolution of the 95% bounds in determining c_0 by using the Fisher formalism applied to AdLIGO. For the cases where the injected EOS is: MS1, H4, MPA1, GNH3 or SQM3. With on the horizontal axis the amount of measurements combined and on the vertical axis the value of c_0 with its associated spread.

In figure 16 can be seen how the EOSs, which are also present in the extensive analysis, are clearly separated and distinguishable after combining ≈ 30 sources and relative bounds of $\approx 10\%$ are reached after ≈ 50 sources have been 'detected' and combined. Our analysis seems to be reasonably optimistic with these approximations when compared to figure 15. This can be explained by (i) the Fisher matrix underestimating the bounds at low SNRs and (ii) our PDFs being perfectly combinable. Both these two factors decrease the spread in the PDFs, in a non truthful way.

The two EOSs we added to our analysis (MPA1, GNH3), are clearly not distinguishable from the EOSs: SQM3 and H4. This can be understood by realising that $c_0 = \lambda(m_0)$, with $m_0 = 1.4 M_\odot$. In figure 14 is clearly visible how the values of $\lambda(m_0)$ for H4 and GNH3 and for SQM3 and GNH3 are very similar. Since our analysis seems to be optimistic in comparison with [7], we do not expect similar EOSs to be measurable with an extensive analysis either. Something that also has to be taken into account is the fact that the predicted amount of BNSs detected per year, in the case of AdLIGO at design sensitivity, lies in the domain $[0.27 - 8.6]$ [37]. In the light of this, combining 200 sources seems to be a little optimistic. The, by [7] predicted, ≈ 50 sources necessary to distinguish between a stiff, moderate and soft equation of state, seems to be reachable when the AdLIGO/AdVIRGO detectors are operational for a period of several years.

7.4.1   Conclusions

Although our Fisher formalism does not arrive at exactly the same results as the extensive analysis, the following similar conclusions can be drawn for determining the EOS, regarding AdLIGO at design sensitivity.

- c_1 and c_2 are deemed unmeasurable.

- By determining c_0 for several dozen NSs, a stiff, moderate and soft EOS can be distinguished. This requires an AdLIGO/AdVIRGO network at design sensitivity to be up and running for several years. Differences between similar EOSs are deemed unmeasurable.

According to these similar conclusions, we deem ourselves justified to regard our Fisher analysis as a rough indication in determining the distinguishability of several EOSs. Particularly with the prospect of ET being less biased when applied to our Fisher formalism, due to its higher SNRs, we expect the results presented in the next section to be an even better resemblance of reality.

7.5   Fisher-ET

In the case of our Fisher analysis applied to ET, c_0 and c_1 are deemed clearly measurable and c_2 to some extent, which would mean a significant increase in our knowledge of the EOS. The evolution of the EOS coefficients is visualised in figures 17, 18 and 19.
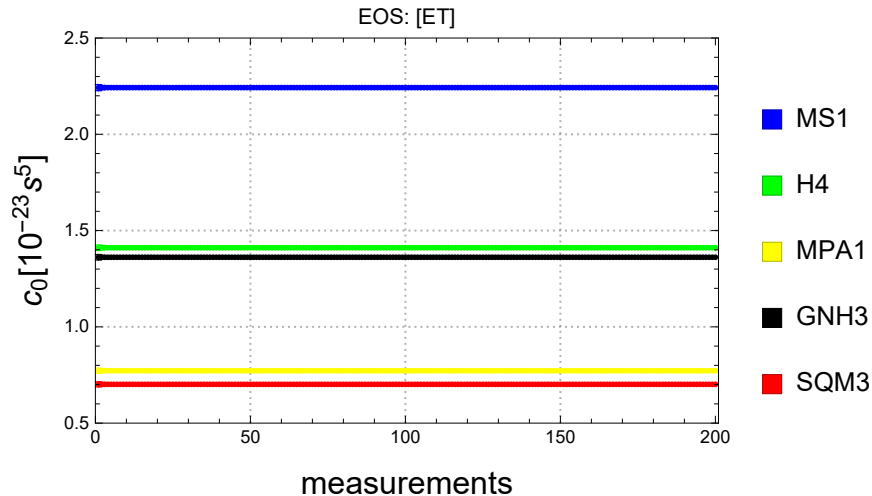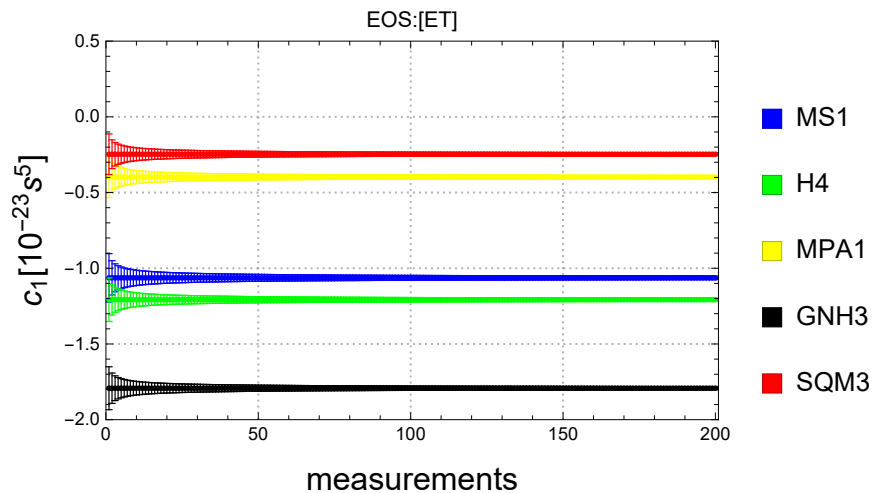
Figure 17: Evolution of the 95% bounds in determining c_0 by using the Fisher formalism applied to ET, for the cases where the injected EOS is: MS1, H4, MPA1, GNH3 or SQM3. With on the horizontal axis the amount of measurements combined and on the vertical axis the value of c_0 with its associated spread. The vertical axis has been re-scaled relative to figures 15 and 16, to visualise the gap between the similar EOSs. For a similar axis scale as in figures 15 and 16, see figure 26 in the appendix.

In figure 17 can be seen how all inserted EOSs are clearly separated and distinguishable after just one detection. This early distinguishability happens because all inserted EOSs have relative bounds smaller than $\approx 2\%$ after just one detection. This results in accurate knowledge of the EOS for some reference mass $m_0 = 1.4 M_\odot$.

Figure 18: Evolution of the 95% bounds in determining c_1 by using the Fisher formalism applied to ET, for the cases where the injected EOS is: MS1, H4, MPA1, GNH3 or SQM3. With on the horizontal axis the amount of measurements combined and on the vertical axis the value of c_1 with its associated spread.

In figure 18 can be seen how all inserted EOSs are clearly separated and distinguishable after

≈ 20 detections and how, after ≈ 50 detections, relative bounds of $\approx 5\%$ can be determined. This results in accurate knowledge of the average slope of $\lambda(m)$.
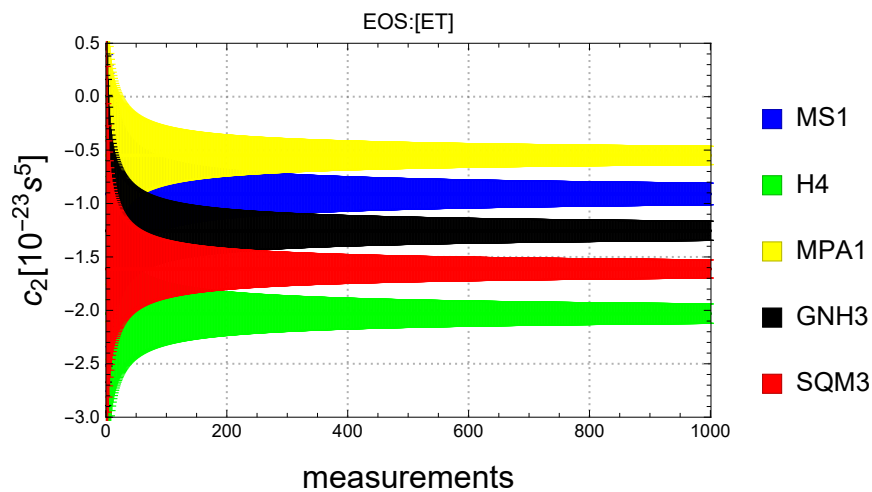

Figure 19: Evolution of the 95% bounds in determining c_2 by using the Fisher formalism applied to ET, for the cases where the injected EOS is: MS1, H4, MPA1, GNH3 or SQM3. With on the horizontal axis the amount of measurements combined and on the vertical axis the value of c_2 with its associated spread.

In figure 27 in the appendix is visualised how the evolution of c_2 takes place up to 200 sources. But, due to the fact that the predicted amount of BNSs detected per year, in the case of ET at design sensitivity, lies in the domain $[1.1 \times 10^3, 2.7 \times 10^4]$ [37], we have expended figure 19 to visualise the combination of 10^3 measurements.

In figure 19 can be seen how all inserted EOSs are clearly separated and distinguishable after ≈ 500 detections, and how, after ≈ 1000 detections, relative bounds smaller than 15% can be determined. This results in some knowledge of the change in slope of $\lambda(m)$.

7.5.1   Conclusions

We can conclude from this analysis that ET will inevitably result in a significant increase in the distinguishability of several EOSs due to the greater sensitivity, larger frequency bandwidth and significant increase in detection rates, relative to 2G detectors. The c_0 and c_1 are expected to be determinable to great accuracy with only information of the early-inspiral of a few BNSs. Determining c_2 to some extent, with only information of the early-inspiral, would necessitate hundreds of BNS detections, which is not unreasonable for ET.

The certainty of these claims, again, stands or falls with the Fisher matrix. But, since our AdLIGO case derived similar results as a more extensive analysis, we predict our ET case to be reasonably reliable in indicating the distinguishability of several EOSs and the accuracy to which the EOS coefficients are determinable.

8   Conclusions

In this thesis we analysed to what extent ET will improve on 2G detectors, , because of its greater sensitivity and larger frequency bandwidth, regarding (i) measuring deviations from GR and (ii) measuring the EOS coefficients that describe the NS EOS. To analyse these problems, we first gained knowledge on GWs, its detectors and an analysis method called the Fisher matrix, as described in chapters 2, 3, 4 and 5.

In chapter 2 we derived a restricted PN waveform up to 3.5PN, which describes the early-inspiral up to the ISCO frequency.

In chapter 3 we discussed the functioning of interferometric GW detectors, the sources of noise they have to endure, the resulting sensitivity of various 1G, 2G and 3G detectors, in the form of the PSD, and their corresponding (predicted) detection rates.

In chapter 4 we discussed the derivation of the Fisher matrix, which gives us an indication of the spread in measured parameter values that can be expected when a GW signal is detected. We also gain knowledge on when the Fisher matrix is a good and a biased approximation.

In chapter 5 we generalise this Fisher formalism to make it applicable to a network of detectors, such as ET.

With the combined knowledge on these subjects we were able to execute our two analyses.

In chapter 6 we analysed to what extent possible deviations from GR are expected to be measurable by ET at design sensitivity, relative to current detectors AdLIGO/AdVIRGO, evaluating only the early-inspiral. We concluded that the construction of ET will inevitably lead to significantly tighter bounds on the testing parameters, by which deviations from GR are measured. With use of the Fisher matrix we expect these bounds to be in the range of [0.1,1] % for lower PN orders and [1,10] % for higher PN orders, when evaluating high SNR, long inspiral binaries. Real measurements by the AdLIGO AdVIRGO network have derived these bounds to be in the range of [10,100] % for lower PN orders and $[100, \rightarrow\rangle$ % for higher PN orders, when evaluating high SNR, long inspiral binaries. We conclude that a resulting increase in measurability of the testing parameters by a factor [10,100] can be expected when ET reaches its design sensitivity.

In chapter 7 we analysed to what extent the EOS coefficients, which describe the NS EOS, are expected to be measurable by ET at design sensitivity, relative to current detectors AdLIGO/AdVIRGO. We conclude that the construction of ET will inevitably lead to a significant increase in the distinguishability of several possible EOSs. The coefficients c_0 and c_1 are expected to be determinable to great accuracy, with information of the early-inspiral of a few BNSs. The coefficient c_2 is expected to be determinable to some extent, with information of the early-inspiral of hundreds of BNSs. Due to the expected increased detection rates for ET, this is not unreasonable.

Note that all these results have been derived using the Fisher matrix that underestimates bounds for low SNRs. Therefore we have confined ourselves to orders of magnitude.

9   Discussion and Outlook

Our Fisher formalism can ofcourse still be improved. We will now give some suggestions for future research with the Fisher matrix.

- One could expand the waveform model to include spin parameters. This will also result in the inclusion of dipole-monopole tidal effects, as described in section 7.1.

- One could include a -1PN testing parameter, in the case of testing GR. This would enable one to constrain the presence of dipole radiation during inspiral [6].

- One could try to model a combination of AdLIGO and AdVIRGO, including sky locations and orientations of actual measurements. This would enable one to compare a Fisher analysis to an actual measurement as correctly as possible.

- One could include non-flat prior distributions, to analyse the effect of these on the subsequently derived PDFs.

- One could analyse NSBH binaries, as we neglected these during this thesis.

- One could combine several GR tests based on multiple detections, as done in [5, 6]. We have only combined analyses in the case of our NS EOS analysis.

However, even when one would include all these modifications, the Fisher matrix will always be a rough analysis method. To accurately analyse the future capabilities of ET, better analysis methods will have to be developed that are capable of processing ET resembling signals that continue for days. Until then, Fisher will remain a rough but useful method for analysing the capabilities of future detectors.

10   ACKNOWLEDGEMENTS

References

[1] B. Abbott, R. Abbott, T. Abbott, M. Abernathy, F. Acernese, K. Ackley, C. Adams, T. Adams, P. Addesso, R. Adhikari, et al., Physical Review Letters **116** (2016), ISSN 1079-7114, URL http://dx.doi.org/10.1103/PhysRevLett.116.061102.

[2] B. Abbott, R. Abbott, T. Abbott, F. Acernese, K. Ackley, C. Adams, T. Adams, P. Addesso, R. Adhikari, V. Adya, et al., Physical Review Letters **119** (2017), ISSN 1079-7114, URL http://dx.doi.org/10.1103/PhysRevLett.119.161101.

[3] M. Maggiore, C. V. D. Broeck, N. Bartolo, E. Belgacem, D. Bertacca, M. A. Bizouard, M. Branchesi, S. Clesse, S. Foffa, J. García-Bellido, et al., Journal of Cosmology and Astroparticle Physics **2020**, 050–050 (2020), ISSN 1475-7516, URL http://dx.doi.org/10.1088/1475-7516/2020/03/050.

[4] C. Van den Broeck, personal communication (2020).

[5] B. Abbott, R. Abbott, T. Abbott, S. Abraham, F. Acernese, K. Ackley, C. Adams, R. Adhikari, V. Adya, C. Affeldt, et al., Physical Review D **100** (2019), ISSN 2470-0029, URL http://dx.doi.org/10.1103/PhysRevD.100.104036.

[6] B. Abbott, R. Abbott, T. Abbott, F. Acernese, K. Ackley, C. Adams, T. Adams, P. Addesso, R. Adhikari, V. Adya, et al., Physical Review Letters **123** (2019), ISSN 1079-7114, URL http://dx.doi.org/10.1103/PhysRevLett.123.011102.

[7] M. Agathos, J. Meidam, W. Del Pozzo, T. Li, M. Tompitak, J. Veitch, S. Vitale, and C. Van Den Broeck, Physical Review D **92** (2015), ISSN 1550-2368, URL http://dx.doi.org/10.1103/PhysRevD.92.023012.

[8] A. Einstein, Königlich Preußische Akademie der Wissenschaften (Berlin) (1918).

[9] J. B. Hartle, *Gravity: An Introduction to Einstein's General Relativity* (2003), ISBN 0805386629, URL http://www.amazon.com/exec/obidos/redirect?tag=citeulike07-20&path=ASIN/0805386629.

[10] B. S. Sathyaprakash and S. V. Dhurandhar, Phys. Rev. D **44**, 3819 (1991), URL https://link.aps.org/doi/10.1103/PhysRevD.44.3819.

[11] C. Cutler and E. Flanagan, Physical Review D **49**, 2658–2697 (1994), ISSN 0556-2821, URL http://dx.doi.org/10.1103/PhysRevD.49.2658.

[12] C. Van den Broeck, *lecture notes of master level course on gravitational waves* (2019), URL https://www.nikhef.nl/~vdbroeck/GW_cursus/.

[13] B. S. Sathyaprakash and B. F. Schutz, Living Reviews in Relativity **12** (2009), ISSN 1433-8351, URL http://dx.doi.org/10.12942/lrr-2009-2.

[14] B. F. Schutz, *A FIRST COURSE IN GENERAL RELATIVITY* (Cambridge Univ. Pr., Cambridge, UK, 1985).

[15] T. W. Baumgarte and S. L. Shapiro, Phys. Today **64N10**, 32 (2011).

[16] K. Arun, B. Iyer, B. Sathyaprakash, and P. Sundararajan, Physical Review D - PHYS REV D **71** (2005).

[17] *Ligo website:what is an interferometer?*, URL `https://www.ligo.caltech.edu/page/what-is-interferometer`.

[18] *Ligo website: If a gravitational wave stretches the distance between the ligo mirrors, doesn't it also stretch the wavelength of the laser light?*, URL `https://www.ligo.caltech.edu/page/faq`.

[19] *Ligo website:ligo's laser*, URL `https://www.ligo.caltech.edu/page/laser`.

[20] D. M. Macleod, S. Fairhurst, B. Hughey, A. P. Lundgren, L. Pekowsky, J. Rollins, and J. R. Smith, Classical and Quantum Gravity **29**, 055006 (2012), ISSN 1361-6382, URL `http://dx.doi.org/10.1088/0264-9381/29/5/055006`.

[21] T. Christopoulos, O. Tsilipakos, G. Sinatkas, and E. E. Kriezis, Optics Express **27**, 14505 (2019), ISSN 1094-4087, URL `http://dx.doi.org/10.1364/OE.27.014505`.

[22] R. Nawrodt, A. Zimmer, T. Koettig, C. Schwarz, D. Heinert, M. Hudl, R. Neubert, M. Thürk, S. Nietzsche, W. Vodel, et al., Journal of Physics: Conference Series **122**, 012008 (2008), URL `https://doi.org/10.1088%2F1742-6596%2F122%2F1%2F012008`.

[23] M. Maggiore, *Gravitational Waves: Volume 1: Theory and Experiments*, Gravitational Waves (OUP Oxford, 2008), ISBN 9780198570745, URL `https://books.google.nl/books?id=mk-1DAAAQBAJ&pg=PA532&lpg=PA532&dq=laser+power+ligo+MW&source=bl&ots=n3hUyIVsvw&sig=ACfU3U0TPCAwRUPasswZOAMho-HgxtxFyg&hl=nl&sa=X&ved=2ahUKEwj1yvmluLjpAhVMKewKHTXGAR4Q6AEwD3oECAYQAQ#v=onepage&q=laser%20power%20ligo%20MW&f=false`.

[24] A. Freise and K. Strain, Living Reviews in Relativity **13** (2010), ISSN 1433-8351, URL `http://dx.doi.org/10.12942/lrr-2010-1`.

[25] GWIC-3G-Committee, GWIC-3G-RD-Team, and International-3G-Science-Team-Consortium (2019), URL `https://gwic.ligo.org/3Gsubcomm/documents/GWIC_3G_R_D_Subcommittee_report_July_2019.pdf`.

[26] L. McCuller, C. Whittle, D. Ganapathy, K. Komori, M. Tse, A. Fernandez-Galiana, L. Barsotti, P. Fritschel, M. MacInnis, F. Matichard, et al., Phys. Rev. Lett. **124**, 171102 (2020), URL `https://link.aps.org/doi/10.1103/PhysRevLett.124.171102`.

[27] S. A. Hughes and K. S. Thorne, Physical Review D **58** (1998), ISSN 1089-4918, URL `http://dx.doi.org/10.1103/PhysRevD.58.122002`.

[28] S. Hild, M. Abernathy, F. Acernese, P. Amaro-Seoane, N. Andersson, K. Arun, F. Barone, B. Barr, M. Barsuglia, M. Beker, et al., Classical and Quantum Gravity **28**, 094013 (2011), ISSN 1361-6382, URL `http://dx.doi.org/10.1088/0264-9381/28/9/094013`.

[29] D. Martynov, E. Hall, B. Abbott, R. Abbott, T. Abbott, M. Abernathy, K. Ackley, C. Adams, P. Addesso, R. Adhikari, et al. (2016).

[30] T. Li, F. Aguilar Sandoval, M. Geitner, C. Gianpietro, V. Dolique, J. Degallaix, R. Flaminio, D. Forest, M. Granata, C. Michel, et al., Physical Review D **89** (2013).

[31] P. Barriga, D. Blair, D. Coward, J. Davidson, J. Dumas, E. Howell, L. Ju, L. Wen, C. Zhao, D. McClelland, et al., Classical and Quantum Gravity (2013).

[32] J. Aasi, B. P. Abbott, R. Abbott, T. Abbott, M. R. Abernathy, K. Ackley, C. Adams, T. Adams, P. Addesso, and et al., Classical and Quantum Gravity **32**, 074001 (2015), ISSN 1361-6382, URL `http://dx.doi.org/10.1088/0264-9381/32/7/074001`.

[33] T. Regimbau, T. Dent, W. Del Pozzo, S. Giampanis, T. G. F. Li, C. Robinson, C. Van Den Broeck, D. Meacher, C. Rodriguez, B. S. Sathyaprakash, et al., Physical Review D **86** (2012), ISSN 1550-2368, URL `http://dx.doi.org/10.1103/PhysRevD.86.122001`.

[34] M. Punturo (originally ET-0106C-10, 2011), URL `http://www.et-gw.eu/index.php/etdsdocument`.

[35] C. Berry, B. O'Reilly, M. Razzano, S. Fairhurst, and P. J. Sutton, Public LIGO Documents (2014).

[36] G. Koekoek, *Et psd fit*, personal communcation (2019).

[37] V. Baibhav, E. Berti, D. Gerosa, M. Mapelli, N. Giacobbo, Y. Bouffanais, and U. N. Di Carlo, Physical Review D **100** (2019), ISSN 2470-0029, URL `http://dx.doi.org/10.1103/PhysRevD.100.064060`.

[38] C. Röver, R. Meyer, and N. Christensen, Classical and Quantum Gravity **28**, 015010 (2010), URL `https://doi.org/10.1088%2F0264-9381%2F28%2F1%2F015010`.

[39] *Classical Models of Light* (John Wiley Sons, Ltd, 2019), chap. 2, pp. 19–64, ISBN 9783527695805, URL `https://onlinelibrary.wiley.com/doi/abs/10.1002/9783527695805.ch2`.

[40] R. Balasubramanian, B. S. Sathyaprakash, and S. V. Dhurandhar, Phys. Rev. D **53**, 3033 (1996), URL `https://link.aps.org/doi/10.1103/PhysRevD.53.3033`.

[41] M. Vallisneri, Physical Review D **77** (2008), ISSN 1550-2368, URL `http://dx.doi.org/10.1103/PhysRevD.77.042001`.

[42] E. Berti, A. Buonanno, and C. M. Will, Physical Review D **71** (2005), ISSN 1550-2368, URL `http://dx.doi.org/10.1103/PhysRevD.71.084025`.

[43] M. L. Chan, C. Messenger, I. S. Heng, and M. Hendry, Physical Review D **97** (2018), ISSN 2470-0029, URL `http://dx.doi.org/10.1103/PhysRevD.97.123014`.

[44] J. Meidam, K. W. Tsang, J. Goldstein, M. Agathos, A. Ghosh, C.-J. Haster, V. Raymond, A. Samajdar, P. Schmidt, R. Smith, et al., Physical Review D **97** (2018), ISSN 2470-0029, URL http://dx.doi.org/10.1103/PhysRevD.97.044033.

[45] T. G. F. Li, W. Del Pozzo, S. Vitale, C. Van Den Broeck, M. Agathos, J. Veitch, K. Grover, T. Sidery, R. Sturani, and A. Vecchio, Physical Review D **85** (2012), ISSN 1550-2368, URL http://dx.doi.org/10.1103/PhysRevD.85.082003.

[46] W. R. Inc., *Mathematica, Version 12.1*, URL https://www.wolfram.com/mathematica.

[47] M. Maggiore, *Gravitational Waves: Volume 2: Astrophysics and Cosmology* (OUP Oxford, 2018), ISBN 9780191074479, URL https://books.google.nl/books?id=FGdRDwAAQBAJ.

[48] B. Abbott, R. Abbott, T. Abbott, S. Abraham, F. Acernese, K. Ackley, C. Adams, R. Adhikari, V. Adya, C. Affeldt, et al., Physical Review X **9** (2019), ISSN 2160-3308, URL http://dx.doi.org/10.1103/PhysRevX.9.031040.

[49] W. Del Pozzo, T. G. F. Li, M. Agathos, C. Van Den Broeck, and S. Vitale, Physical Review Letters **111** (2013), ISSN 1079-7114, URL http://dx.doi.org/10.1103/PhysRevLett.111.071101.

[50] T. Damour, A. Nagar, and L. Villain, Physical Review D **85** (2012), ISSN 1550-2368, URL http://dx.doi.org/10.1103/PhysRevD.85.123007.

[51] L. S. Collaboration, *detections of gravitational waves to date*, URL https://www.ligo.org/detections.php.
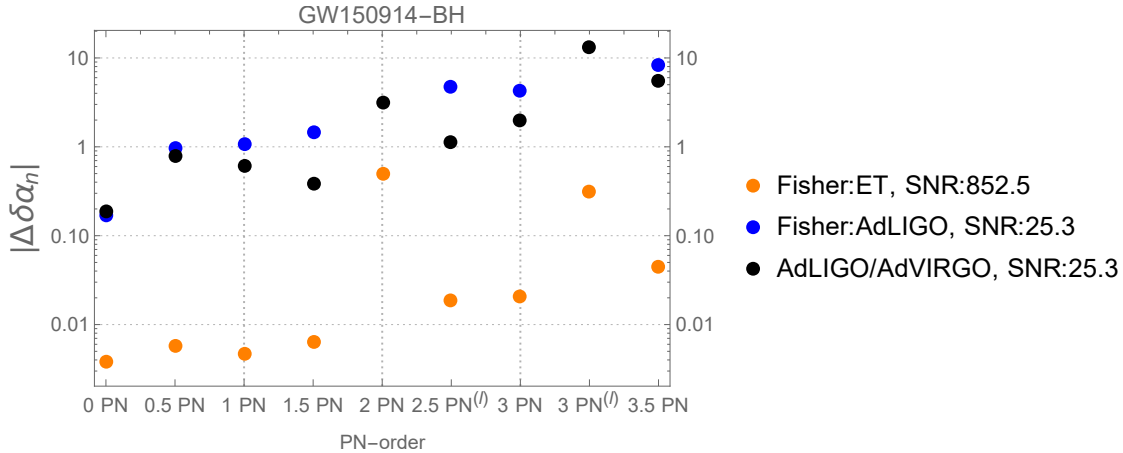
A   APPENDIX

A.1   Tests of general relativity

Figure 20: 90% upper bounds $|\delta\hat\alpha_n|$ on the absolute magnitude of the testing parameters for GW151226 ($m_1 = 35.6 M_\odot, m_2 = 30.6 M_\odot, d = 440$ Mpc) [48] determined by: (i) the Fisher matrix adjusted to resemble ET at design sensitivity, (ii) the Fisher matrix based on the AdLIGO design sensitivity, but re-scaled to resemble the (iii) analysis based on the actual AdLIGO/AdVIRGO detection, as described in [5], using the IMRPhenomPv2 waveform. Note that these are relative deviations (except for the 0.5PN term).
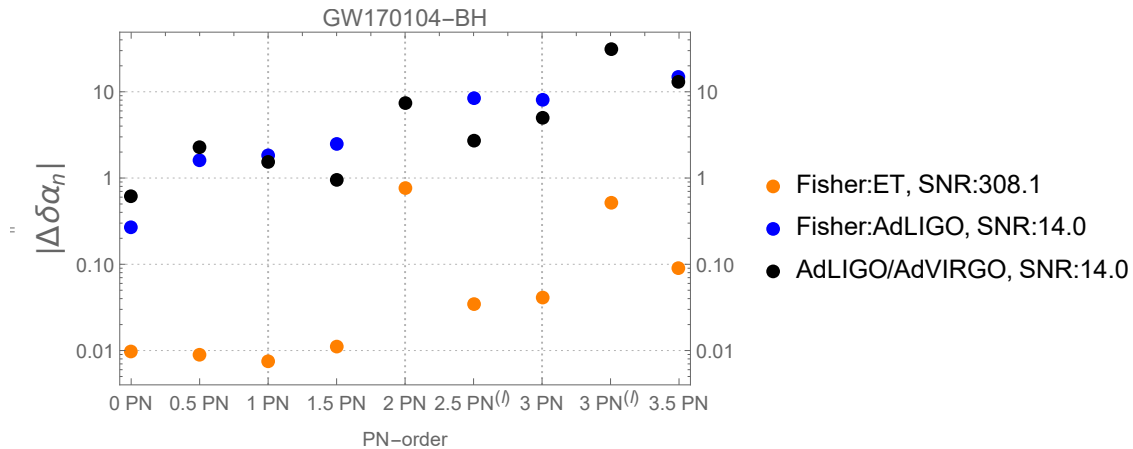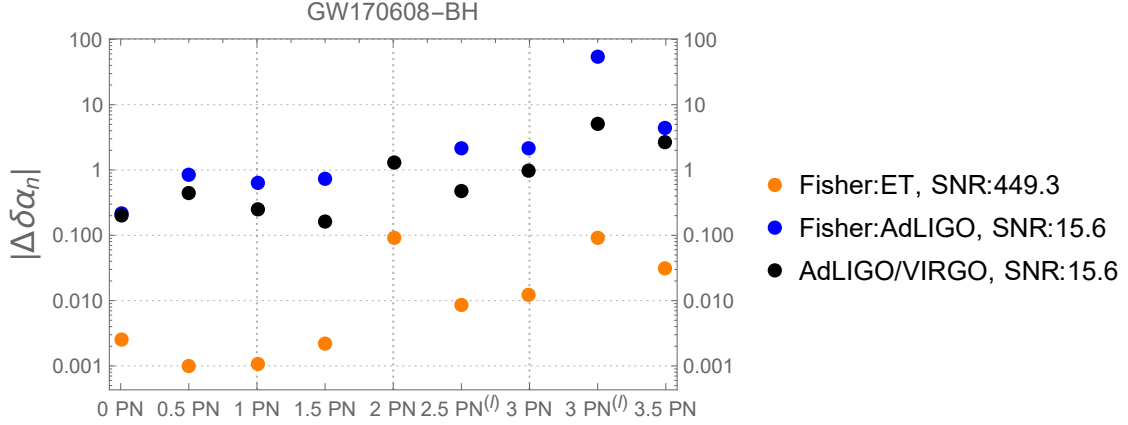

Figure 21: 90% upper bounds $|\delta\hat\alpha_n|$ on the absolute magnitude of the testing parameters for GW150914 ($m_1 = 30.8 M_\odot, m_2 = 20.0 M_\odot, d = 990$ Mpc) [48] determined by: (i) the Fisher matrix adjusted to resemble ET at design sensitivity, (ii) the Fisher matrix based on the AdLIGO design sensitivity, but re-scaled to resemble the (iii) analysis based on the actual AdLIGO/AdVIRGO detection, as described in [5], using the IMRPhenomPv2 waveform. Note that these are relative deviations (except for the 0.5PN term).
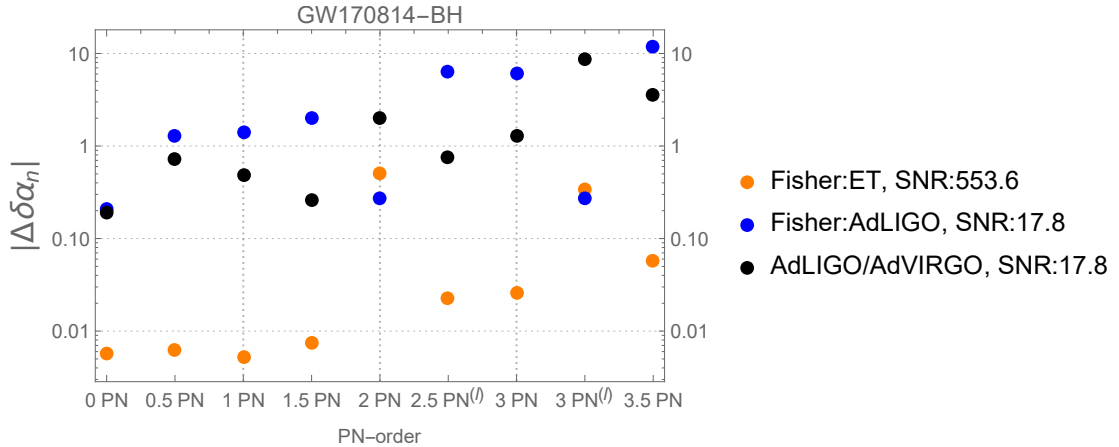
Figure 22: 90% upper bounds $|\delta\hat{\alpha}_n|$ on the absolute magnitude of the testing parameters for GW170608 ($m_1 = 11.0 M_\odot, m_2 = 7.6 M_\odot, d = 320$ Mpc) [48] determined by: (i) the Fisher matrix adjusted to resemble ET at design sensitivity, (ii) the Fisher matrix based on the AdLIGO design sensitivity, but re-scaled to resemble the (iii) analysis based on the actual AdLIGO/AdVIRGO detection, as described in [5], using the IMRPhenomPv2 waveform. Note that these are relative deviations (except for the 0.5PN term).

Figure 23: 90% upper bounds $|\delta\hat{\alpha}_n|$ on the absolute magnitude of the testing parameters for GW170814 ($m_1 = 30.6 M_\odot, m_2 = 25.2 M_\odot, d = 600$ Mpc) [48] determined by: (i) the Fisher matrix adjusted to resemble ET at design sensitivity, (ii) the Fisher matrix based on the AdLIGO design sensitivity, but re-scaled to resemble the (iii) analysis based on the actual AdLIGO/AdVIRGO detection, as described in [5], using the IMRPhenomPv2 waveform. Note that these are relative deviations (except for the 0.5PN term).

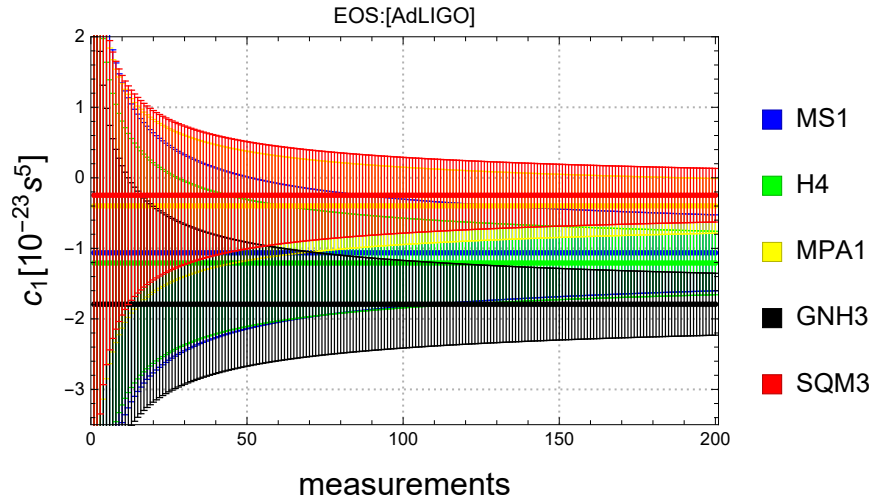## A.2   Tests of neutron star equation of state

Figure 24: Evolution of the 95% bounds in determining c_1 by using the Fisher formalism applied to AdLIGO, for the cases where the injected EOS is: MS1, H4, MPA1, GNH3 or SQM3. With on the horizontal axis the amount of measurements combined and on the vertical axis the value of c_1 with its associated spread.
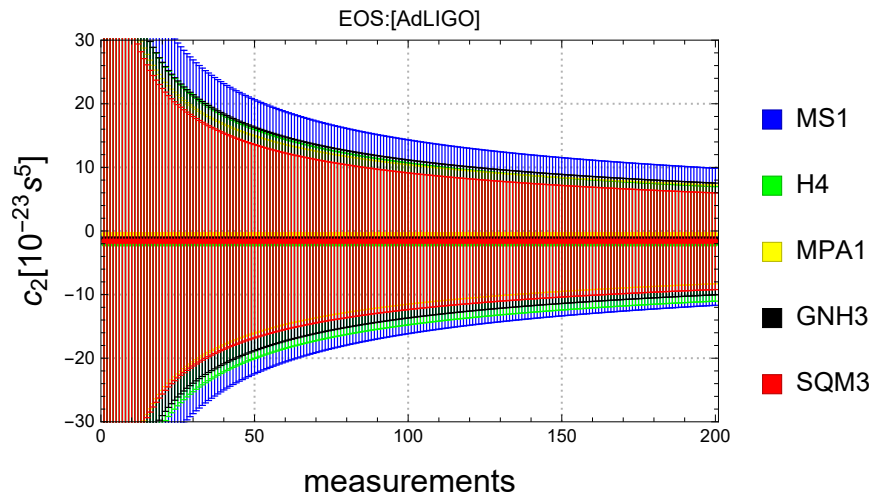

Figure 25: Evolution of the 95% bounds in determining c_2 by using the Fisher formalism applied to AdLIGO, for the cases where the injected EOS is: MS1, H4, MPA1, GNH3 or SQM3. With on the horizontal axis the amount of measurements combined and on the vertical axis the value of c_2 with its associated spread.
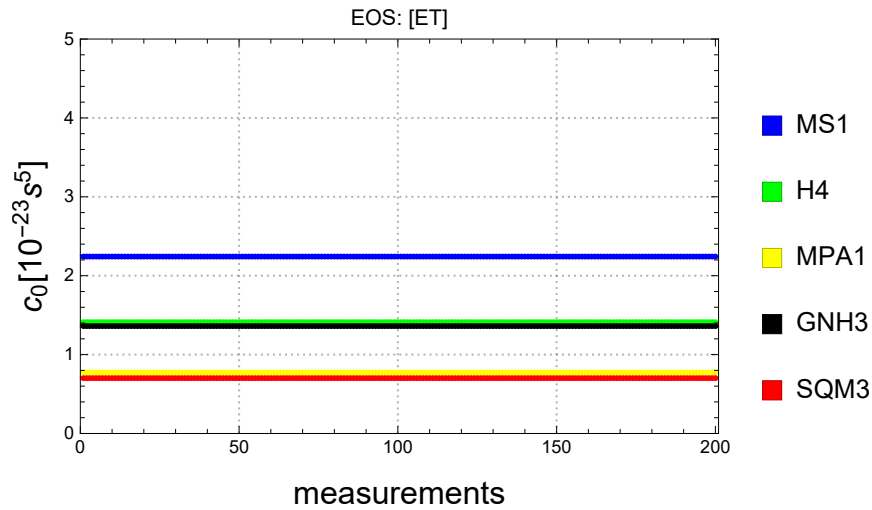
Figure 26: Evolution of the 95% bounds in determining c_0 by using the Fisher formalism applied to ET, for the cases where the injected EOS is: MS1, H4, MPA1, GNH3 or SQM3. With on the horizontal axis the amount of measurements combined and on the vertical axis the value of c_0 with its associated spread.
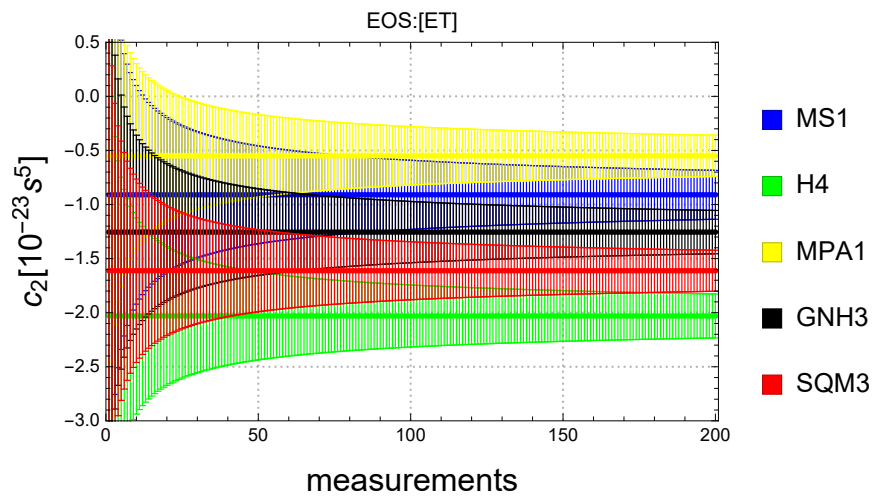

Figure 27: Evolution of the 95% bounds in determining c_2 by using the Fisher formalism applied to ET, for the cases where the injected EOS is: MS1, H4, MPA1, GNH3 or SQM3. With on the horizontal axis the amount of measurements combined and on the vertical axis the value of c_2 with its associated spread.